CHALMERS
UNIVERSITY OF TECHNOLOGY

Software Defined Radio for Medical Applications

Master's thesis in Master Biomedical Engineering

LAURA GUERRERO

Department of Electrical Engineering
CHALMERS UNIVERSITY OF TECHNOLOGY
Gothenburg, Sweden 2019

Master's thesis 2019:EENX30

Software Defined Radio for Medical Applications

LAURA GUERRERO

CHALMERS
UNIVERSITY OF TECHNOLOGY

Department Electrical Engineering
Division of Signal Processing and Biomedical Engineering
Biomedical Electromagnetics
Chalmers University of Technology
Gothenburg, Sweden 2019

Software Defined Radio for Medical Applications

Laura Guerrero

Supervisor: Xuezhi Zeng, Signals and systems
Examiner: Andreas Fhagel, Signal and systems

Master's Thesis 2019:EENX30
Department of Electrical Engineering
Division of Signal Processing and Biomedical Engineering
Biomedical electromagnetics group
Chalmers University of Technology
SE-412 96 Gothenburg
Telephone +46 31 772 1000

Cover: USRP2901 Software Defined Radio Device

Gothenburg, Sweden 2019

Software Defined Radio for Medical Applications
Laura Guerrero
Department of Electrical Engineering
Chalmers University of Technology

Abstract

A portable, cheap and accurate system is necessary for pre-hospital diagnosis, and recently software defined radio technology (SDR), has attracted the interest of researchers for these same reasons. The objective of this master thesis is to evaluate the feasibility of using SDR technologies for Medical applications. In this project, the parameters that affect the measurement quality were studied. Furthermore, calibration strategies for random phase offset between the transmitter and the receiver were successfully developed and evaluated. Then the measurement repeatability and accuracy of the system were evaluated, the results show that the calibration system made the measurements repeatable, making the system practical for medical monitoring. On the other hand, in order to achieve higher accuracy, the calibration methods need to be further developed. Additionally, the possibility of using the SDR for other medical application was explored, the results show that it can be effectively used in non-contact vital sign monitoring.

Keywords: SDR,medical applications, vital sign detection,measurement repeatability, measurement accuracy,medical diagnosis.

Acknowledgements

I would like to express my deepest gratitude to my supervisor, Xuezhi Zeng, thank you for so patiently answering my questions and for guiding me in right direction. It would have been impossible to accomplish this work without your warm and kind help. You are a role model.

I would like to thank my parents and my brother for their support and kindness, I would have not been able to accomplish my goals without the constant motivation you gave me.

My special thanks to my friends from the Study Room: Asta, Mauricio, Isabel, Berglind, Tryggvi, Alberto, Ryan, Abdul and Alex. You created an unforgettable time in my life and I will be forever thankful for the support I received from you.

Laura Guerrero, Gothenburg, June 2019

Contents

List of Figures

1
Introduction

In this section, Ultra Wide Band (UWB) microwave imaging is introduced including a background and current imaging methods.

1.1 Background

Traditional imaging systems used for diagnostic, like Magnetic Resonance Imaging (MRI) and X-ray Computed Tomography (CT), are powerful but normally only available in hospitals. Conditions affecting circulation and pressure in the brain, like stroke, are life threatening, and in these cases the sooner treatment is applied, to restore the circulation and pressure, the greater the likelihood of recovery. This is the reason why a pre-hospital diagnostic system is necessary.

The rapid development of microwave integrated circuit technology has allowed the size and cost of microwave electronics to be dramatically reduced, so microwave-based devices are particularly suitable for pre-hospital diagnostic systems [1].

Microwave for biomedical imaging has been broadly studied in the past years for stroke, trauma and breast cancer detection [1–4]. Microwave diagnostics relies on the existence of dielectric contrast between healthy tissues and lesions. Often we consider only permittivity and conductivity and ignore permeability, as biological tissue is in general non-magnetic.

Several studies have found that the permittivity of cancerous breast tissue is higher than normal breast tissue and also higher than non-malignant breast tumors [5, 6]. Other studies have analyzed the dielectric properties of the brain and found a difference in permittivity and conductivity between white and gray matter [7]. Moreover, it has been found that the dielectric properties of brain tissue declines with age [8, 9].

Normally the tissues studied are healthy tissues but diseases and injuries might lead to changes in dielectric properties [1]. An example of such change is the coagulation of blood while bleeding. Another example is the case during an ischemic stroke where the dielectric properties will change due to loss of circulation [10].

1.2 Microwave Imaging Approaches

In microwave imaging techniques, an electromagnetic wave is used to illuminate the object that is being tested. Scattering will happen because of natural dielectric variations of the tissue. Two approaches can be taken: Tomographic methods and

radar-based techniques [3]. In tomographic imaging methods the measured scattering data is used to quantitatively reconstruct spatial representation of the dielectric profile of the tissue.

A nonlinear Reconstruction algorithm, such as the conjugate gradient algorithm is used [4, 11]. The algorithm's objective is to minimize a penalty function of the difference between the measured signal and a simulated signal, obtained by using the finite-difference time domain method or finite element method [12]. This minimization is accomplished by iteractively updating the dielectric parameters in the model. Since these algorithms can be computationally demanding, reconstruction times can become unfeasible. For 2-D imaging the reconstruction times are reasonable but for 3-D reconstruction reconstruction times can be several hours in supercomputers.

In radar-based imaging method, an UWB signal illuminates the object from different directions. Unlike Tomography, where the objective is to get a quantitative reconstruct of a spatial representation of the dielectric profile of the scattering targets; the objective of radar imaging is to use the amplitude and echo time to detect and position strong scatterers, such as tumors by using simple delay-and sum algorithms [13].

This reconstruction strategy is similar to a global positioning receiver, where the position is determined by triangulating using propagation times from different directions [1].

1.3 Current Imaging System Setups

The measurements of UWB data for microwave imaging, can be carried out in the frequency domain or the time domain. Microwave imaging system are normally constructed using lab intruments. Many experimental systems for biomedical imaging use frequency domain measurement systems, and usually they are based on Vector Network Analyzers (VNA) [4, 11, 12, 14]. The VNA is a powerful measurement platform that provides a high accurate measurement solution in experimental uses. The VNA uses the stepped frequency modulations technique to perform measurements in wide frequency bands, in each frequency step, a sinusoidal signal will illuminate the object, the scattered signals are received by the VNA and the scattering parameters will be calculated.

There are also experimental setups working in time domain consisting of a pulse generator and an real-time or sampling oscilloscope [15–18].The pulse generator is used to illuminate the object and the oscilloscope measures the time domain response.

1.4 Motivation and Project aim

Among all the microwave systems that have been investigated for medical imaging, most of them are based on lab-instrument, which are bulky and expensive. A portable, cheap and accurate system is crucial for promoting the development of microwave technology, especially for pre-hospital applications.

Most recently, a new type of system that has been mainly employed for radio communications has attracted interest from researchers in this field [19, 20]. This system is based on software defined radio technology (SDR) and the whole system is built on a single circuit board which consists of a radio frequency integrated circuit (RFIC) transceiver and a digital signal processing (DSP) unit.

The aim of this master thesis project is to investigate a compact and cheap SDR board for medical applications. The main objectives include:

- Configure the board for required measurement.
- Investigate parameters that affect the measurement quality.
- Develop and evaluate calibration strategies for random phase offset between the transmitter and the receiver.
- Investigate measurement repeatability and accuracy for medical diagnosis.
- Study the possibility of using the SDR for other medical applications.

1.5 Thesis Outline

The main content of the thesis is summarized here: Chapter 1 gives an overall introduction to the topic and the project motivation and aim. Chapter 2, gives an overview of microwave imaging for medical applications. Chapter 3, introduces conventional UWB measurement technologies. In Chapter 4, the parameters that affect the measurement quality are studied, calibration strategies are developed and evaluated, and the repeatability of the system is evaluated. In Chapter 5, the accuracy of the measurements is evaluated. In Chapter 6, the possibility of using the SDR for other medical applications is explored.

2

Microwave Measurement for Medical Diagnostics

In this chapter an introduction to microwave measurements for medical diagnosis is presented. Additionally, two conventional technologies for utra wide band (UWB) measurements are introduced: time domain and frequency domain technologies. The architecture of each system are presented and the measurement strategies described in detail.

2.1 Microwave Measurement for Medical Diagnostics

A common antenna configuration scenario is shown in Figure 2.1. The antennas are placed around the object that is going to be tested and each antenna transmits a waveform that will help illuminate the object. The scattered waveform will be received by antennas and subsequently measured.

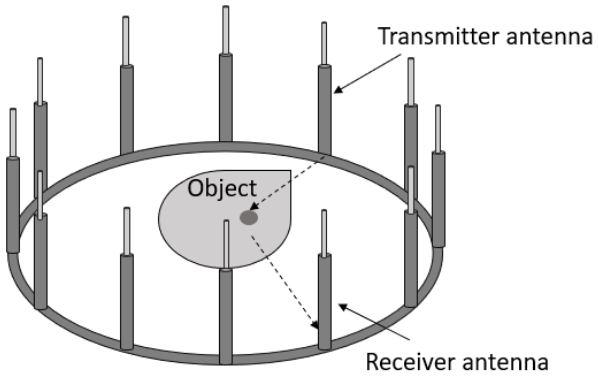

Figure 2.1: Measurement configuration for medical diagnostics.

The choice of frequency band is generally a trade-off between penetration depth and imaging resolution. A higher frequency can result in a better resolution, but experience greater attenuation when penetrating to human tissue, which are very lossy. In order to achieve a good resolution and a sufficient penetration depth, a wide frequency spectrum is needed. This is the reason why there is interest in using

UWB technology in medical applications. Specifically, a system may be classified as an UWB system when its operating frequency range is wider than 500 MHz or 20 fractional bandwidth [21]. With this technique the higher frequencies are used to increase the resolution in the reconstructed image, allowing to resolve finer structures, and the lower frequencies will allow the imaging of larger structures and high contrast objects [3]. In microwave tomography, the lower frequencies are necessary as the initial guess for proceeding iteration, since scattered data is non-linearly related to the scattering target and the higher the frequency, the higher is the non-linearity [4].

2.2 Measurement Technology

The UWB microwave measurements systems for medical diagnostics are usually built from instruments found in laboratories. The measurements can be divided in two strategies: time domain measurements, using a pulse generator and an oscilloscope [15] and frequency domain measurements using a VNA.

2.2.1 Time Domain Measurements

Time domain measurements system consist of a pulse generator (a step source) and a real-time or sampling oscilloscope to measure the scattered signal, Figure 2.2 shows an example of a time domain measurement system used for experiments with breast phantom imaging.

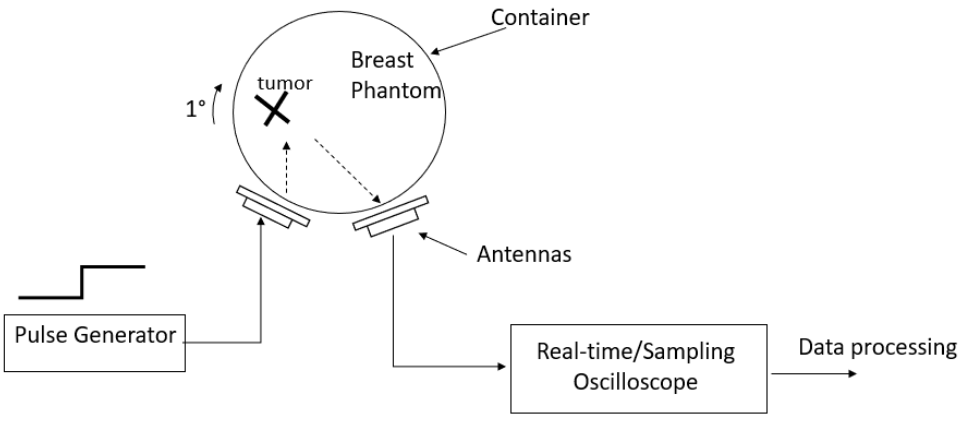

Figure 2.2: Time domain measurement system.

2.2.1.1 Pulse Generator

The pulse generator is fundamental in a time domain UWB imaging system. Pulse generators provide a number of pulse shapes, the pulse shapes can be classified into the following categories: rectangular, gaussian impulse, gaussian monocycle pulse (first derivative of the gaussian impulse signal [21]), and step [16]. The spectral energy will be defined by the pulse shape.

The classical pulse generation techniques are discrete RF transistor, avalanche transistor, step-recovery diode (SRD) and tunnel diode [17]. Nonlinear transmission lines (NLTLs) and analog/digital monolithic microwave integrated Circuits (MMIC) can be used to build ultra-fast risetime and high amplitude pulse generators [22]. According to time-frequency relation, the bandwidth required for microwave medical imaging corresponds to a pulse with duration less than hundred picoseconds (ps) [17].

To generate picosecond pulses, SRD and NLTLs are frequently used [23, 24]. SRD is used in many pulse generator designs for UWB applications, since it presents a simple, compact and low-cost solution [18, 25].

2.2.1.2 Real Time/Sampling Oscilloscope

Modern digital oscilloscopes can be divided in two categories depending on how they operate: real-time oscilloscopes and sampling (or equivalent time) oscilloscopes [26].

A real-time sampling oscilloscope captures an entire waveform on each trigger event, for this reason a large number of data points must be captured in one continuous record. Generally this type of system uses interleaving of multiple analog-to-digital converters (ADCs) in parallel, in order to increase the converters effective sample rate [27]. Normally real-time oscilloscopes have high input impedance and are devised to measure voltages inside electrical circuits operating in real time. The bandwidth of the oscilloscopes is limited to 500 MHz [26].

In the equivalent time sampling oscilloscope, the effective sample rate of the ADC can be extended beyond the nominal sampling rate of the ADC [17]. Instead of dealing with the whole signal in real time, the equivalent time sampling oscilloscope collects samples of the instantaneous voltage of the input signal on successive samples and will construct the samples to form a picture of the waveform [28]. There are two types of equivalent sampling: sequential sampling and random sampling.

A detailed description of random sampling can be found in [29]. In sequential sampling oscilloscopes, the stroboscopic technique is used. The stroboscopic technique is the one used to slow down the motion (or frequency) of events which are too fast to observe by conventional means [29]. In other words a slow replica of the signal will be assembled from individual measurements of many repetitions of the signal (as shown in Figure 2.3).

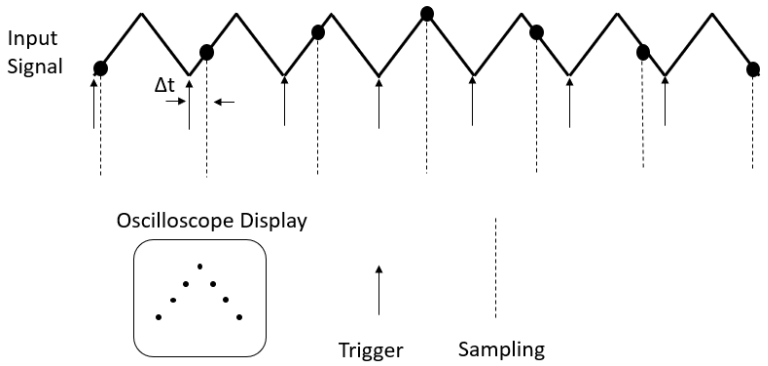

Figure 2.3: Sequential sampling oscilloscope.

In the first measurements cycle the signal is measured at the starting point $T = T_0$. Then a sequential delay (Δt) is added at each cycle. In the second measurement cycle, the amplitude is measured at time $T = T_0 + \Delta t$, the third measurement cycle is measured at time $T = T_0 + 2\Delta t$. This process will be repeated until the entire pulse length is sampled.

Sampling oscilloscopes have a higher accuracy than real time oscilloscopes, since they have a higher effective sampling than the real time oscilloscope, meaning that they have smaller aliasing errors. However, the measurement time is determined by the sample rate and the number of sample points, and sampling oscilloscopes reconstruct the waveform from many repetitive measurements. Consequently, sampling oscilloscopes have higher measurement accuracy at the expense of measurement speed [17].

2.2.2 Frequency Domain Measurements

The frequency domain measurements can be divided in two strategies: frequency modulated continuous wave (FMCW) [30], and stepped frequency continuous wave (SFCW) [19].

2.2.2.1 Frequency Modulated Continuous Wave (FMCW)

In a FMCW radar a chirp signal is used, a chirp signal is a signal in which the frequency increases or decreases with time (frequency ramp). The chirp signal is generated with a constant amplitude sinusoidal signal whose frequency is linearly swept in a band over a specific time, the signal generated can be expressed with the Equation 2.1 [31]

$$s(t) = \cos\left(2\pi(f_0 t + \frac{f_1 - f_0}{2T}t^2)\right), \tag{2.1}$$

Where f_0 is the starting frequency, f_1 is the final frequency and T is the time it takes to sweep from f_0 to f_1.

In a traditional FMCW radar, the chirp is transmitted, it propagates at the speed of light and will hit the target after a propagation delay, the signal then

bounces back and is received by the receiving antenna after another time delay. It is then mixed with the instantaneous chirp signal, and down-converted, the down-converted signal will have a single tone f_d which is the beat frequency resulting from the time delay between the transmitted and returned signals.

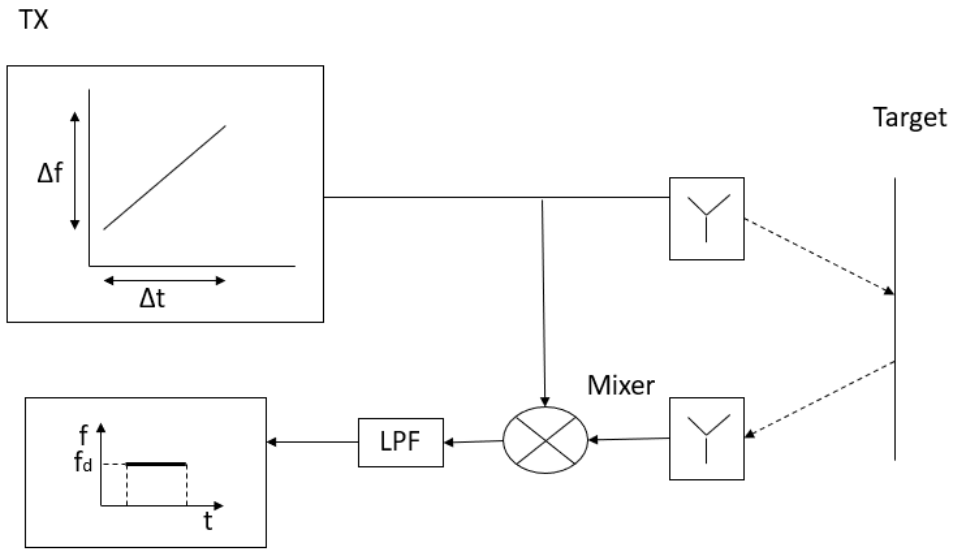

Figure 2.4: Frequency modulated continuous wave radar.

The range of a target can be determined from Equation 2.2:

$$R = \frac{v f_d}{2m}, \tag{2.2}$$

where m is the rate of the frequency sweeping.

The drawback of this technique is that it is difficult to achieve an accurate and constant frequency's sweeping rate over a wide band given the non-linearity of the synthesizer, specially when a voltage-controlled oscillator (VCO) is used instead [32].

2.2.2.2 Stepped Frequency Continuous Wave (SFCW)

SFCW radars transmit successive trains of sinusoidal signals at different frequencies, as shown in Figure 2.5. The transmitted frequencies are separated by a constant frequency step f and the total bandwidth B is N*f where N is the number of steps. PRI is the transmission duration of each sinusoidal signal and the total time to complete the frequency sweep is N PRI [34]. The received signal at each frequency is then down-converted to a intermediate-frequency (IF) signal, which is then further converted into the base-band in-phase (I) and in quadrature (Q) signals, which contain the amplitude and phase information of the targets. Then the I/Q signals are converted into digital signals with an analog-to-digital converter (ADC). The acquired digital data over a wideband is then transformed into a "synthetic pulse" in time domain by using the Inverse Discrete Fourier Transform (IDFT), this pulse depicts the target and can be processed to reveal the target's features [32].

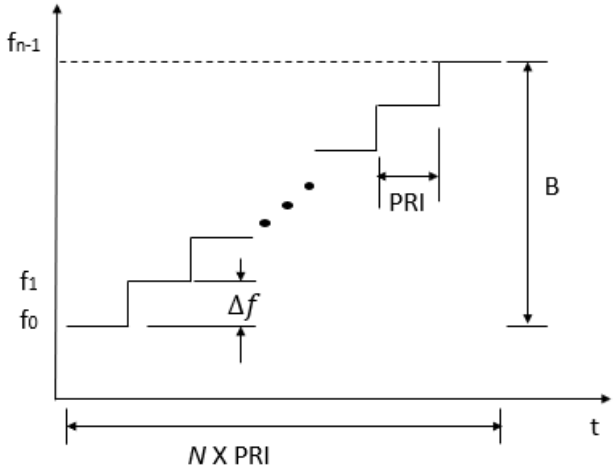

Figure 2.5: Frequency vs time.

This is the measurement strategy employed in VNAs. With VNA measurement, the object response at each frequency is expressed as scattering parameters, which are the ratio of received wave to transmitted wave.

3

Software Defined RF System

As mentioned in Section 2, most of the microwave based medical diagnostic systems are constructed with bulky and expensive laboratory instruments. This is useful for experimental use, however, for pre-hospital diagnosis a small, cheap and accurate system is necessary. For this reason, SDR technology, mainly employed for radio communications, has attracted attention in this field. This chapter gives a introduction of the explored SDR board, USRP2901. The block diagram and functions are described in detail.

3.1 Advantages of SDR Systems

The traditional hardware based radio devices can become limiting for cross functionality and encounter the problem that they can only be modified through physical intervention. This can result in an increased production cost and reduced flexibility in support of multiple waveform standards [33]. The advantage of using SDR is that it presents an efficient and inexpensive solution to all the problems of the traditional hardware based radios. In the SDR the physical layer processing is carried out through adaptable software operating on programmable processing technologies, this includes the field programmable gate arrays (FPGA), digital signal processor (DSP), general purpose processors (GPP), programmable system in chip (SoC). This allows new features to be added to existing radio systems without requiring adding new hardware.

3.2 USRP 2901

The National Instruments universal software radio peripheral (USRP) devices are wideband SDRs which can be used for different RF applications. As shown in Figure 3.1, this board mainly includes a wide band RF transceiver and a FPGA, which are respectively an analog measurement platform and a digital processing unit. The investigated board has a frequency range of 70 MHz to 6 GHz, gain range of 76 dB, and maximum instantaneous real-time bandwidth is of 56 MHz. The transmitter has a maximum output power of 20 dBm and the receiver has a maximum input power of -15 dBm.

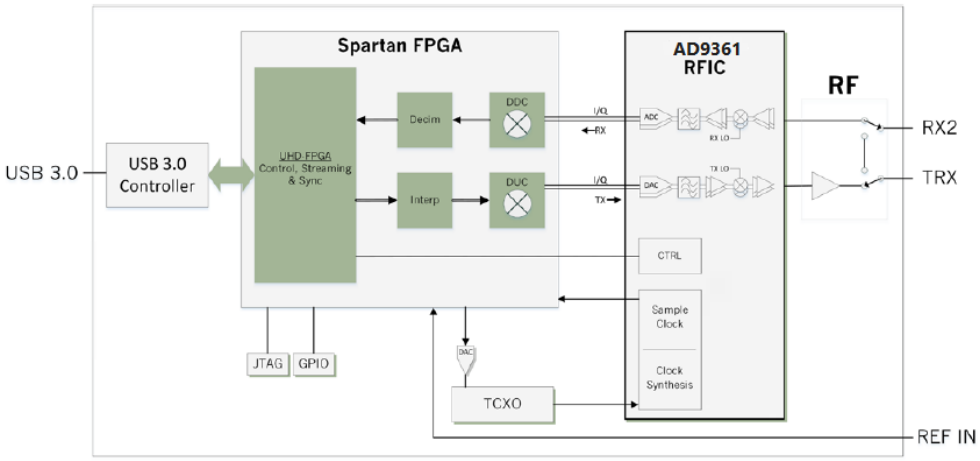

Figure 3.1: Block diagram of USRP [34].

3.2.1 Block Diagram

The block diagram of the board is presented in Figure 3.2. The board is composed of two channels and each channel has two ports, one of the ports can act as either receiver or transmitter and is labeled Tx/Rx1 and the other port labeled Rx2 is a receiving only port.

3.2.1.1 Receiver and Transmitter Path

The transmit path starts with the host computer, it synthesizes base-band IQ signals and transmits the signals to the device over a USB 3.0 or USB 2.0 connection.

Then the digital up-converter (DUC) mixes, filters, and interpolates the I and Q signals to 61.44 MS/s. The Spartan 6 FPGA provides digital up-conversion functionality in the board, which includes fine-frequency tuning and several filters for decimation.

Next the digital-to-analog converter (DAC) converts the data from the I and Q channels. The AD9631 transceiver includes two fully programmable 128-tap FIR filter with interpolation options. The FIR output is sent to a series of interpolation filters that provide additional filtering and data rate interpolation prior to reaching the DAC.

The baseband I and Q signals can be represented with equations 3.1 and 3.2 [35]

$$I = A\cos(\theta) \tag{3.1}$$

$$Q = A\sin(\theta) \tag{3.2}$$

The mixer up-converts the signals to an RF frequency. The PLL controls the VCO to make sure that the device clock and LO can be frequency-locked to a reference signal.

After mixing, the signal becomes [32, 36]:

$$x = A\cos(wt + \theta) = I\cos(wt) + Q\sin(wt), \tag{3.3}$$

where $w = 2\pi f$ and w, θ and A are the RF frequency, phase and amplitude of the transmitted signal.

The received signal can be expressed with Equation 3.4

$$r = B\cos(w(t-\tau)+\theta), \tag{3.4}$$

where B is the amplitude of the received signal and τ the elapsed time between transmission and reception.

The receiver chain begins with a low-noise and drive amplifier to amplify the incoming signal from the port. Next the signal is down-converted by the mixer to the baseband or IF in-phase (I) and quadrature (Q) components. Following this, the I and Q data is digitized by a 12 bit analog-to-digital converter (ADC). Then the FPGA digital down-converter (DDC) mixes, filters, and decimates the signal to a user-specified rate. After decimation, the data is streamed to a host computer over a USB 3.0 or USB 2.0 connection.

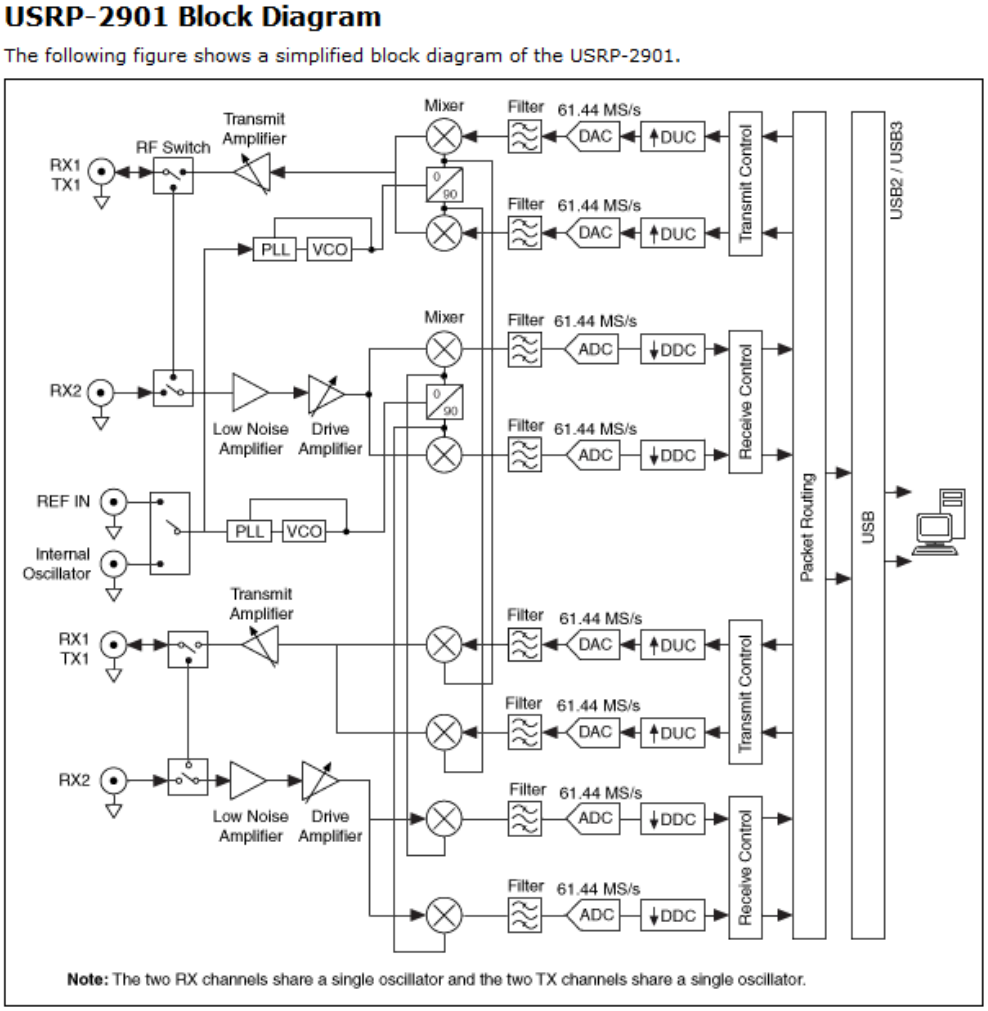

Figure 3.2: Block diagram of the USRP 2901 [37].

3.2.1.2 Internal RF Switch

As it can be seen in Figure 3.2, the RF switches are located after each port. They have two different positions allowing for transmit and receive operations to occur on the same shared port. Having the RF switch presents the advantage of increasing the number of receivers available. It has the disadvantage that the transmitting and receiving port are connected, meaning that there will be greater leakage between ports.

3.2.1.3 RFPLL Synthesizers

The function of the synthesizer is to generate a range of frequencies from a single reference frequency, a carrier frequency to move up the base band signal to a desired RF signal. The transceiver contains two independent RFPLL synthesizers. The PLL synthesizers are of a fractional-N architecture with completely integrated VCO and loop filters.

4

Fundamental Test with the SDR

In this chapter, several fundamental test were performed in order to gain more understanding of the system. Particularly, the measurement repeatability was investigated.

4.1 Power and Gain

As mentioned in Section 3, the receiver has a maximum input power of -15 dBm, it is important that the received power does not go over this limit, to avoid damaging the device during tests. In addition, the good knowledge of power level at different frequencies is the prerequisite for achieving the best measurement quality.

The setup used, for investigating the power, is shown in Figure 4.1. The transmitter/receiver in channel zero (Tx/Rx1) is connected to the transmitter/receiver in channel one (also labeled Tx/Rx1), and a 10 dB RF attenuator is used to protect the receiver from a too high input power.

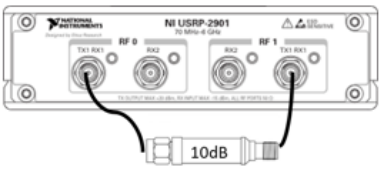

Figure 4.1: Basic measurements setting.

Figure 4.2 displays the magnitude of the received signals at each frequency in the range 500 MHz-6 GHz. It can be seen that the power of the received signal decreases with the frequency, and in this particular image the power drops from -34dB to -50dB in the frequency range 500 MHz-3 GHz, having a -15 dB drop. This is an expected behavior in the device, given the received signal gain changes shown in the specifications of the AD9361 [38].

To improve the measurement quality of weak signals, the gain in the amplifiers must be increased accordingly. However, this may result in the saturation of stronger signals. This is the reason why, a detailed description of the saturation point of the received signals is needed. It was decided that the gain variations would be done on the receiver's amplifier, to avoid damaging the device on the test by exceeding the maximum input power in the receiver.

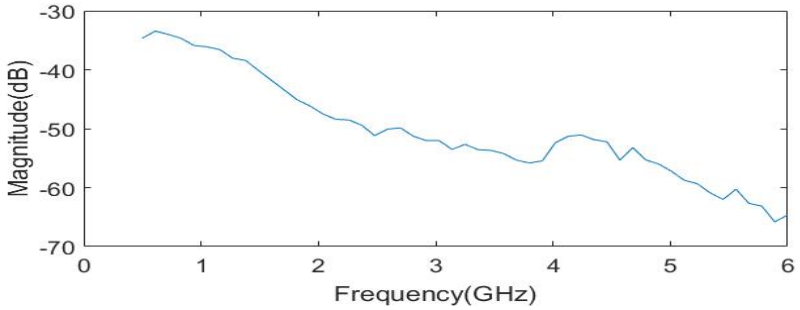

Figure 4.2: Magnitude of signal received from 10dB RF attenuator.

A simple evaluation is done to compare the point of saturation of each frequency band, the test was done with 8 different frequencies (500 MHz, 1 GHz, 1.5 GHz, 2 GHz, 2.5 GHz, 3 GHz, 3.5 GHz and 4 GHz), the received power level for different gain settings were shown in Figure 4.3.

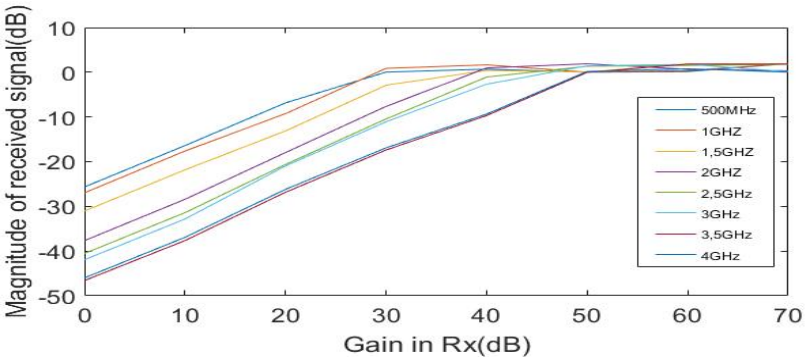

Figure 4.3: Comparison of the gain behavior depending on the frequency.

It can be seen that the saturation occurs at the later position (a higher gain) for a higher frequency, which can be expected from the data shown in Figure 4.2. Figure 4.4 shows an example of a saturated signal. In this example, the gain in the receiver was set to 50 dB and the gain in the transmitter was set to 0 dB.

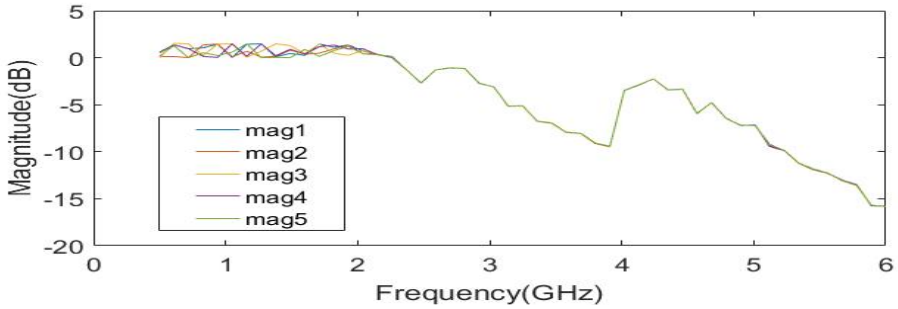

Figure 4.4: Power of received signal when using 50 dB gain.

It is important to point out the noise floor also increases with the gain, as shown in Figure 4.5. However, the increase of the noise floor with the gain is less than that of the power, which consequently resulting in a high signal to noise ratio

(SNR). This conclusion however is only valid when the system operates in the linear region.

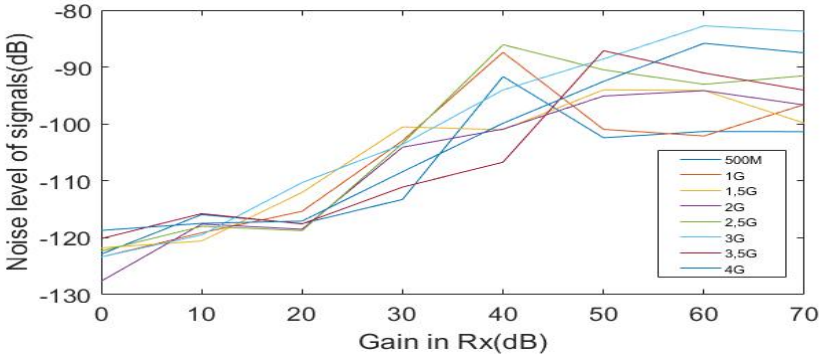

Figure 4.5: Noise level depending on the gain.

4.2 IQ Rate and Noise Level

UWB measurements performed in frequency domain systems require doing a frequency sweeping of a large number of discrete frequency points, which can end up being time consuming. Since there is an increased demand on measurement speed, it is important to study the parameters that will have an effect on the measurement speed. The IQ rate will define how fast samples are taken, so it is important to measure the response from the received signal when this parameter is changed.

In the test, a CW signal at 915 MHz was studied. Both the transmitter and receiver gain were set to 0 dB. Figure 4.6 show the magnitude of the signal and the magnitude of the floor noise level for different IQ settings.The magnitude of the signal will stay stable before reaching an IQ rate higher than 50MHz,where there is a small magnitude drop from -35dB to -38dB. On the contrary, the magnitude of the noise floor will increase with the IQ rate. Therefore, the SNR of the signal decreases as the IQ rate increases. When the IQ rate increases, the duration of acquisition for the measurement will decrease in time. This means that the frequency bin will increase in width, so the noise displayed increases. An example of the difference the IQ rate generates on the signals is shown in Figure 4.7. The Figure displays the IQ data and power spectrum of two different signals with IQ rate 3.5MHz and IQ rate 60MHz. It can be observed that the noise level on the signal will change according to Figure 4.6.

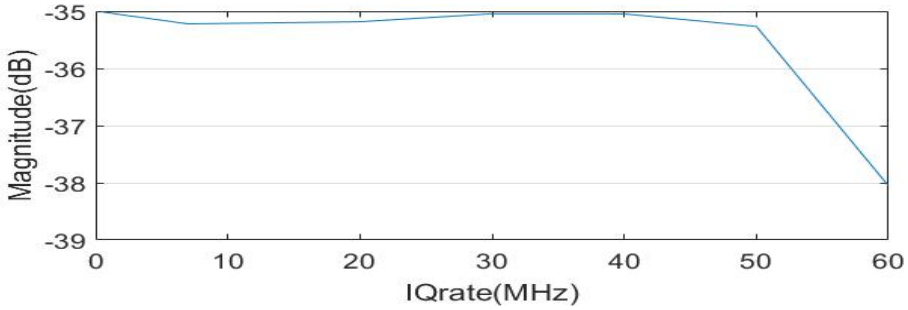

(a) Magnitude of received signal.

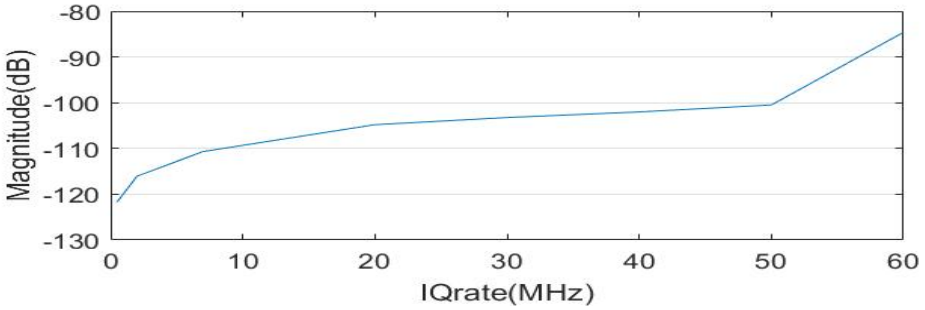

(b) Noise level of received signal.

Figure 4.6: Magnitude of signal and noise level depending on IQ rate.

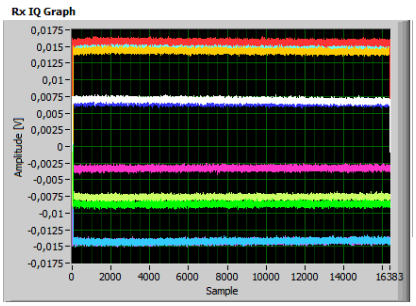

(a) IQ data (3.5MHz).

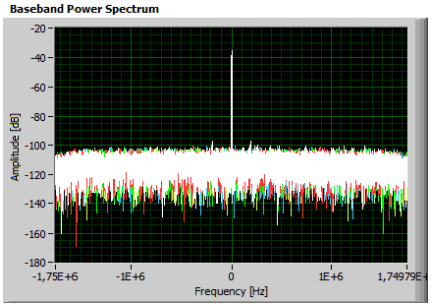

(b) Power spectrum (3.5MHz).

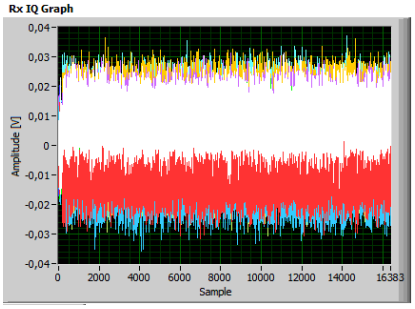

(c) IQ data (60MHz).

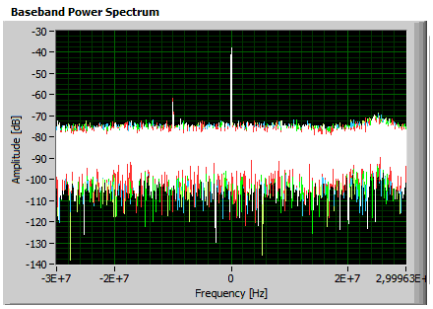

(d) Power spectrum (60MHz).

Figure 4.7: IQ rate and power spectrum.

4.3 Measurement Repeatability

The repeatibility is how much the results of successive measurements will agree, if the same test is done in the same measurement setup. The generation of repeatable experiments is essential in the microwave diagnosis and microwave imaging field. An example is when monitoring is implemented, the repeatability is important, since it is crucial to differentiate between the differences occurring due to object changes, and differences occurring due to the measurement setup.

A fundamental test was performed to investigate the measurement repeatability, and the measurement setup is the same as in Figure 4.1. In the test, a CW signal at 915 MHz was studied. Both the transmitter and receiver gain were set to 0 dB. The I/Q rate in both transmitter and receiver is set to 500kHz. The measurement was done 100 times with the same setup, and the magnitude and phase of the received signal for these 100 measurements were given in Figure 4.8

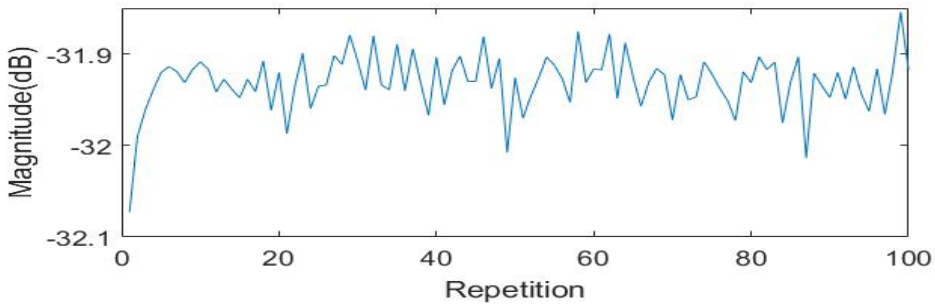

(a) Magnitude

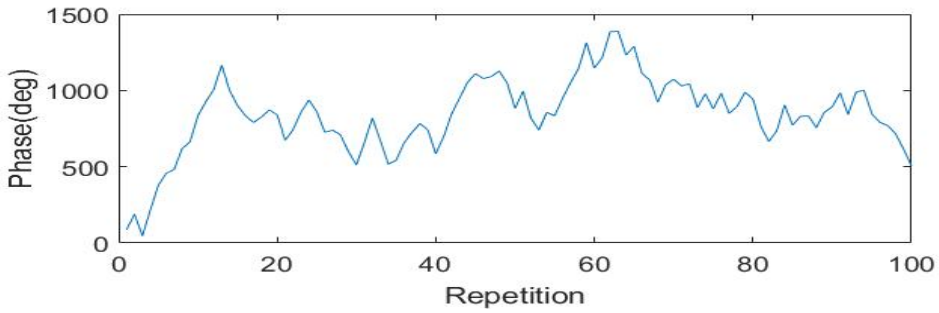

(b) Phase

Figure 4.8: Received magnitude and phase in a 100 repetitions

It can be seen that both the magnitude and phase varies from run to run. While the magnitude changes in a small range, the phase variation is large and completely random. This is due to the internal architecture of the device, as shown in Section 3. In the device, the transmitter and receiver have different PLLs and the phase of the generated clocks are therefore not aligned, resulting a random phase offset from run to run. Therefore, an effective strategy to calibrate the random phase offset is needed.

4.4 Calibration Strategies

To address this repeatibility problem, three calibration strategies are proposed and evaluated in this section. In each calibration strategy, two attenuators (10dB and 6dB) were used, one of them acting as the object and the other acting as the reference line. Since the goal of the calibration is to make the measurement repeatable, the experiment will be repeated many times with the same setup to evaluate the performance of each calibration strategy.

4.4.1 Strategy 1

In this strategy, the idea is to measure the object and the reference with the same physical transmitter and the same physical receiver. In section 3, it was explained that there is one physical receiver in each channel and the internal RF switch can be used to switch between port Tx/Rx1 (that can act as both transmitting and receiving port), and port Rx2 (that is a receiving only port).

The strategy is shown in Figure 4.9. The transmitter in channel 0 is connected to a 3 db power divider, and each of the output ports of the power divider is connected to an attenuator which is further connected to a port in channel 1. With this strategy, the receiver will first be connected to the port Tx/Rx1, measuring signal attenuated by the 10 dB attenuator, then the receiver will switch to the Rx2 port, receiving signal coming from the 6 dB RF attenuator.

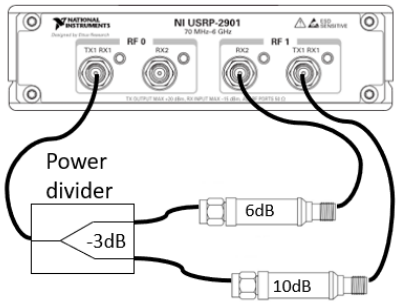

Figure 4.9: Measuremets setup used in strategy 1.

In each test, a frequency sweep was done in the range 500 MHz - 6 GHz,using steps of 110 MHz (50 frequency points). The transmitter sent 16384 sample points, and the two receiving ports (connected to object and reference line), collected 8192 samples each. Both TxGain and RxGain are set 0 dB and the IQ rate is 500 kHz for the transmitter and the receiver.

The test was repeated 20 times, Figure 4.10 shows the magnitude and phase of the relative measurement, which is the ratio of the object data (10 dB) to the reference data (6 dB). No averaging was applied to the measurement data. Figure 4.11 displays the same 20 tests with the data averaged over 5000 samples.

It is shown that both the magnitudes and phases of the relative measurement are stable from run to run, indicating a good repeatability. It can also be seen that

the measurement uncertainty is bigger in the non-averaged case than in the averaged case, and the measurement uncertainty increases in higher frequencies. This can be explained by the power drop experienced in the received signals (Figure 4.2) in higher frequencies, since the signals become much smaller compared to the size of the noise.

The mean value and the standard deviation of the magnitude of the received signals in each frequency is show in Figure 4.12. It can be seen that the SNR of the signal increased 20 dB when averaging was done on the signals. Likewise the mean value and variance of the phases are shown in Figure 4.13. The standard deviation of the phase of the not averaged data can get values as high as 15 degrees in higher frequencies. On the other hand the standard deviation of the averaged data is under 0.2 deg for all frequency points.

The deviation is much smaller in the averaged samples than the non-averaged samples; furthermore, the size of the random noise is bigger in higher frequencies compared to the magnitude of the signal. The averaging of the measurements helped reduce its effect on the data. Since the averaging of the samples improved the measurement uncertainty at all frequencies, the conclusion reached is that this strategy is limited by the size of the random error.

Although this strategy succeeded in stabilizing the magnitude and phase in each frequency point, there are some disadvantages. As the receiver needs to be sequentially switched to two receiving ports during the measurement, the received data includes a transition part which needs to be excluded before the data processing. Furthermore, the received sample points need to be splitted between each receiving session.

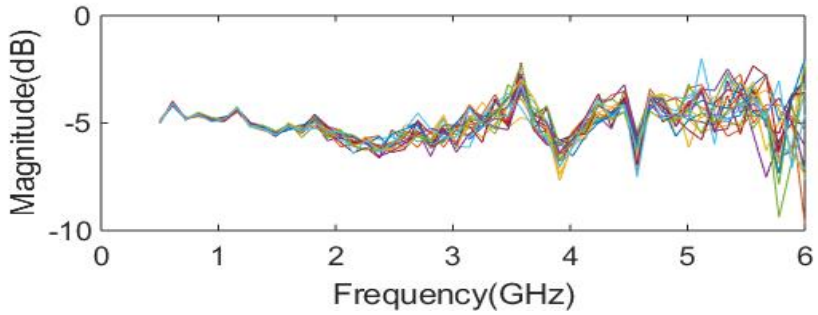

(a) Magnitude of 20 measurements (no averaging).

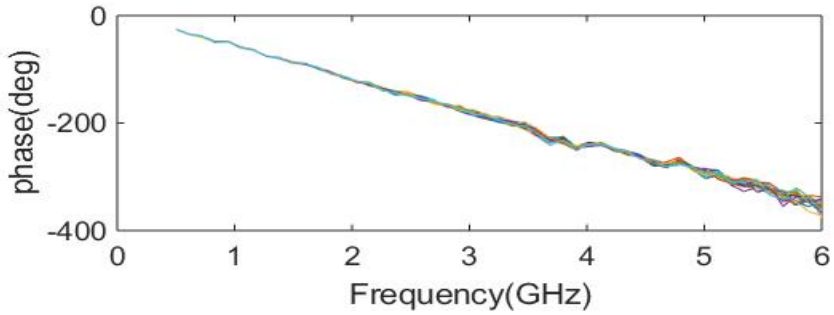

(b) Phase of 20 measurements (no averaging).

Figure 4.10: Magnitude and phases obtained with strategy 1 (not averaged data).

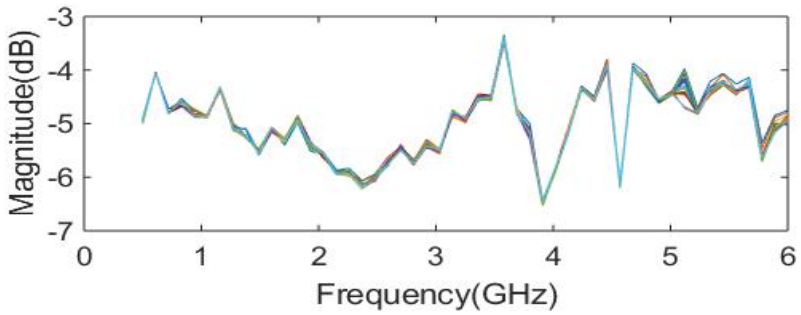

(a) Magnitude of 20 measurements (averaged over 5000 samples).

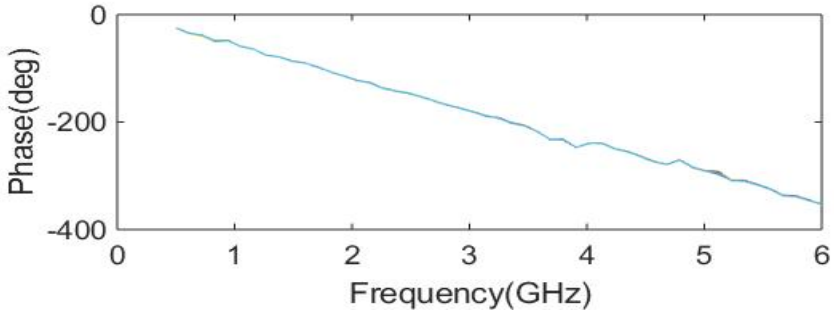

(b) Phase of 20 measurements (averaged over 5000 samples).

Figure 4.11: Magnitude and phases obtained with strategy 1 averaged over 5000 samples.

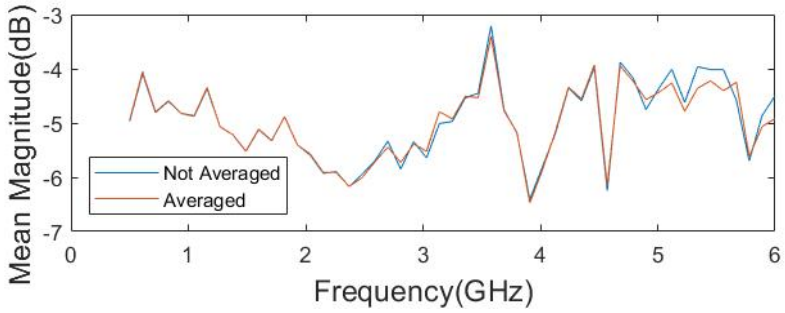

(a) Mean value of magnitude of 20 measurements.

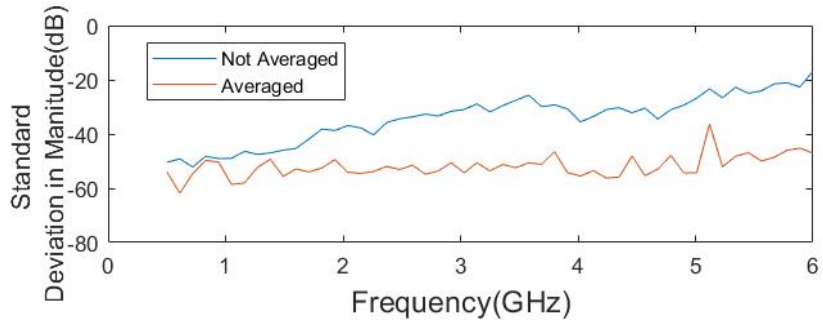

(b) Standard deviation of magnitude of 20 measurements.

Figure 4.12: Mean and standard deviation of magnitude in strategy 1 of averaged and not averaged data.

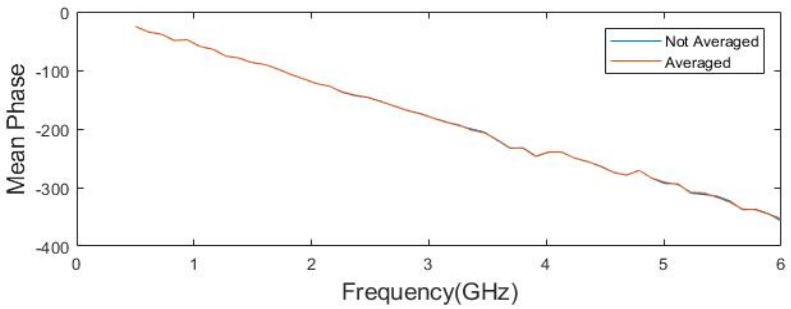

(a) Mean value of the phase of 20 measurements.

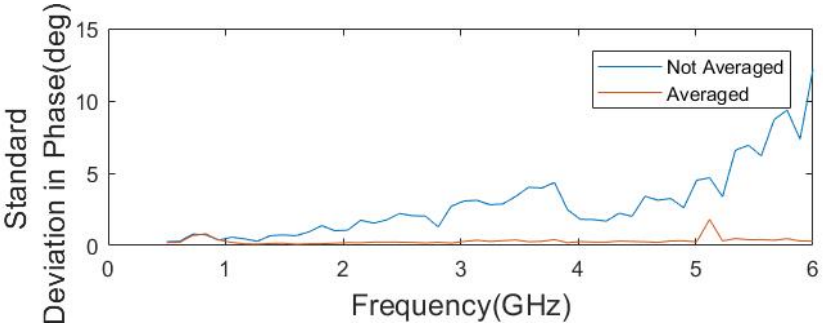

(b) Standard deviation of the phase of 20 measurements.

Figure 4.13: Mean and standard deviation of phase in strategy 1 of averaged and not averaged data.

4.4.2 Strategy 2

To attempt to overcome the problems found in strategy 1, another strategy is implemented. In this strategy, the object signal and the reference signal use different receivers in different channels, this allows to receive in parallel. The strategy works on the assumption that both receivers are identical. Additionally, since the receivers will be located farther apart, then there should be a smaller amount of leakage between them.

The architecture of the RF transceiver in the board does not permit to send a signal from one channel and receive in two different channels. Therefore, the two transmitting channels will be activated, even if only one transmitter is sending data. The unused transmitting port will not send any data and the port will be terminated with a 50 Ω coaxial matched load. This is done to ensure that the transmitter will not interfere with the other signals.

The strategy is shown in Figure 4.14, the transmitter/receiver in channel 0 is connected to a 3 dB power divider, and each of the output ports of the power divider is connected to an attenuator, which is further connected to the receiving only port in each channel. Again, a frequency sweep was done in the range 500 MHz - 6 GHz, using the same settings as in Strategy 1.

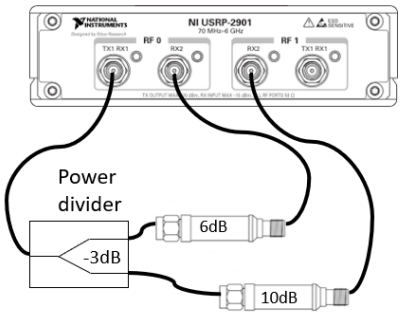

Figure 4.14: Measurement setup used in strategy 2.

The measurements were only repeated 5 times for this strategy, since the repeatability of the measurements was not good. Figure 4.15 shows the magnitude and phase of the relative measurement when no averaging was applied to the measurement data. Likewise Figure 4.16 shows the magnitude and phase of the relative measurement, with data averaged over 1200 samples.

It can be seen that the repeatability of the measurements is not as good as in Strategy 1, since only 5 measurements were done and the value of the magnitude and phase of the relative measurements are stable, but fluctuating in a big margin.

The uncertainty increases with the frequency, just like in Strategy 1. This is reduced by the averaging. It can be seen that the averaging did not help reduce the uncertainty in frequency points under 3 GHz. This happens because this strategy is limited by deterministic noise, therefore, the averaging does not help reduce it. When tested, the receivers did not behave in the same way. This deterministic noise

could be explained by differences in the hardware in both receivers. This difference in hardware will increase the number of error sources, because the end results will have the added error of the difference between the receivers.

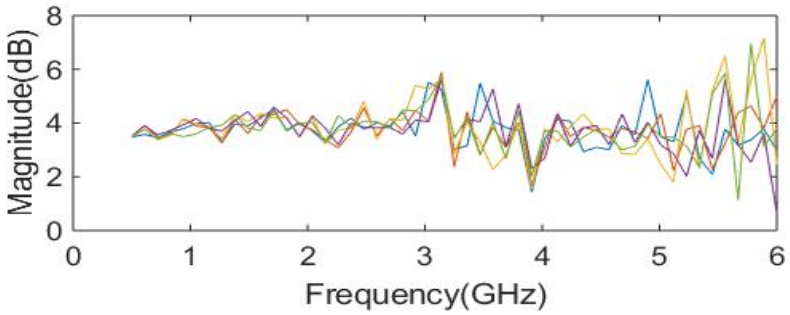

(a) Magnitude of 5 measurements (no averaging).

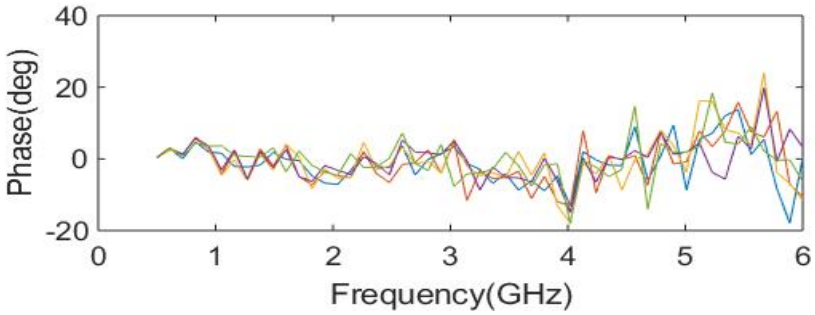

(b) Phase of 5 measurements (no averaging).

Figure 4.15: Magnitude and phases obtained with strategy 2 (not averaged data).

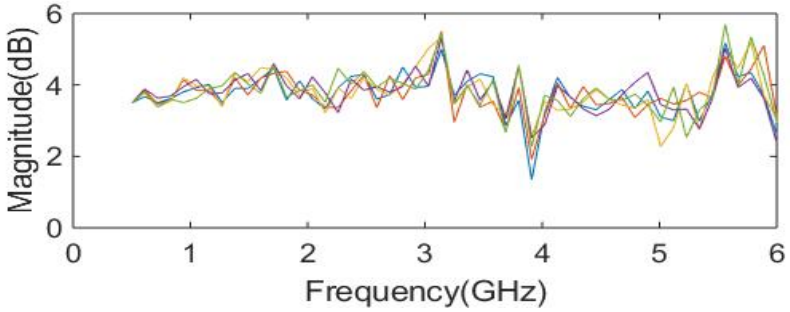

(a) Magnitude of 5 measurements (averaged over 1200 samples).

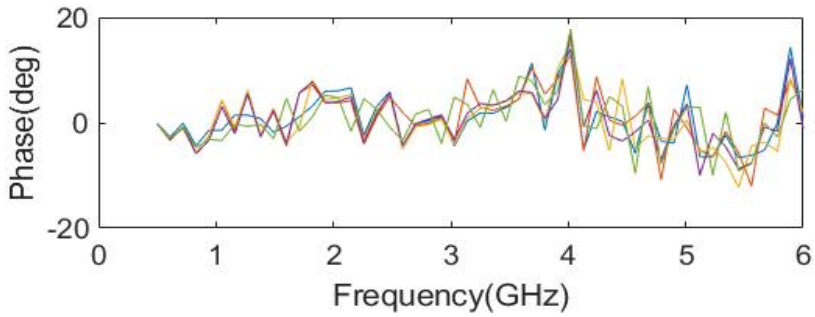

(b) Phase of 5 measurements (averaged over 1200 samples).

Figure 4.16: Magnitude and phases obtained with strategy 2 averaged over 1200 samples.

4.4.3 Strategy 3

Considering the architecture of the board, another strategy similar to strategy 2 was implemented. In this strategy each RF attenuator will be connected to a different channel, this can be seen in Figure 4.17.The setup of the cables change but the program running is the same as in strategy 2. Instead of sending no data in the second channel, The same signal is sent in both transmitters. A frequency sweep with the same settings as the other strategies is done.

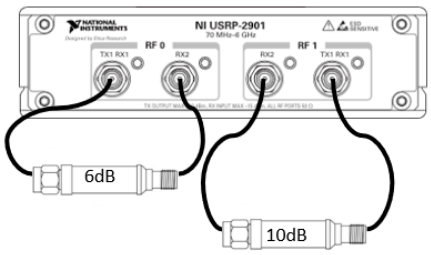

Figure 4.17: Measurement setup used in strategy 3

The measurements were only repeated also 5 times for this strategy, since the results were not as promising as Strategy 1. Figure 4.18shows the magnitude and phase of the relative measurement when no averaging was applied to the measurement data. The magnitude and the phase are better than strategy 2, but still the results are not as good as the results in strategy 1. Figure 4.19 shows the magnitude and phase of the relative measurement, with data averaged over 1200 samples. The averaging helped with the uncertainty increase with the frequency, like in the other strategies, but did not decrease the uncertainty in lower frequencies. The conclusion is that this strategy is limited by deterministic noise and comes from hardware differences. This strategy uses two different transmitters and two different receivers, so there should be more error sources than in strategy 2. Yet, the repeatability of the measurements is better in this strategy than in strategy 2 for an unknown reason to the author.

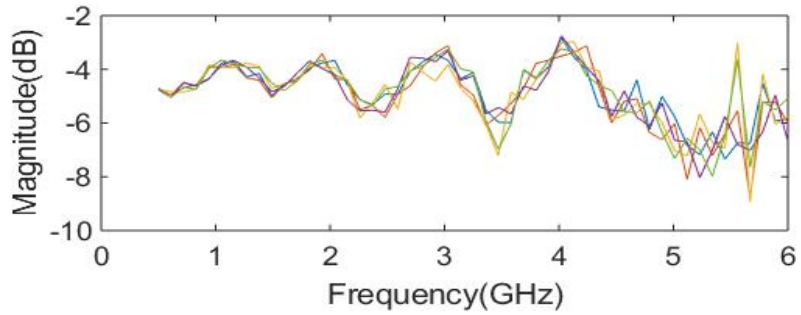

(a) Magnitude of 5 measurements (no averaging).

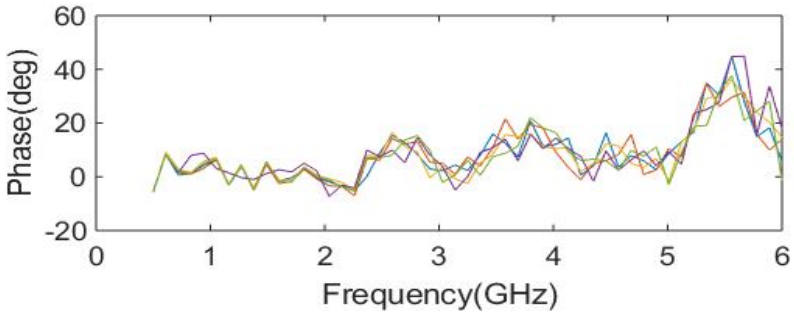

(b) Phase of 5 measurements (no averaging).

Figure 4.18: Magnitude and phases obtained with strategy 3 (not averaged data).

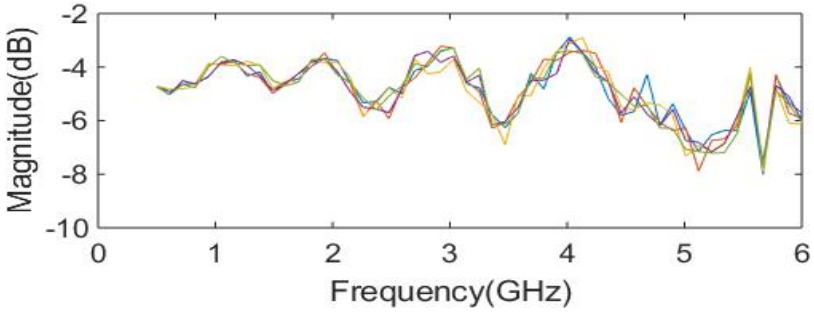

(a) Magnitude of 5 measurements (averaged over 1200 samples).

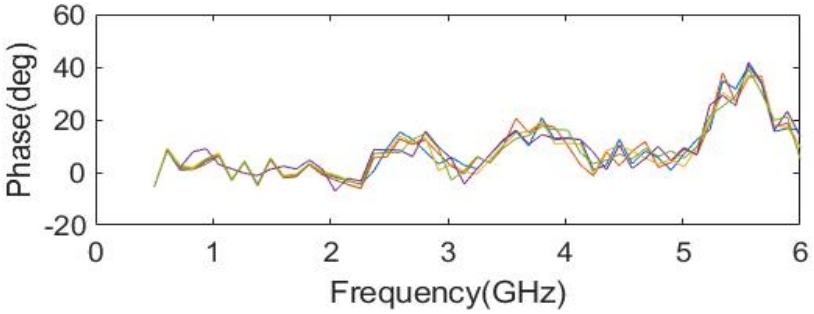

(b) Magnitude of 5 measurements (averaged over 1200 samples).

Figure 4.19: Magnitude and phases obtained with strategy 3 averaged over 1200 samples.

5

Real Measurements

In this chapter, real measurement will be performed in order to evaluate the measurement accuracy.

5.1 Initial accuracy test

The accuracy is how much the values of the measurements are close to the true values. The accuracy of the measurements is important for the image reconstruction in microwave tomography systems, because it is the prerequisite for the successful reconstruction of the internal composition of the object. Figure 5.1 and 5.2 are simple measurement setups to resemble a measurement example for microwave imaging. A power splitter was used to split the power to two RF paths. One is the reference measurement path and other is the object measurement path. In Figure 5.1, the 6 dB attenuator is the measurement object of interest and In Figure 5.2, the measurement object is the 10 dB attenuator.

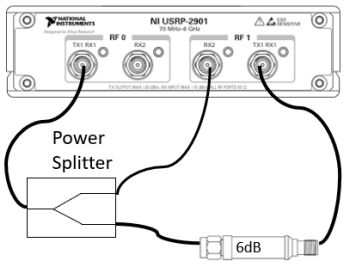

Figure 5.1: Measurement setup using the 6 dB attenuator as object of interest

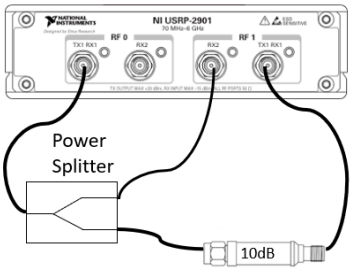

Figure 5.2: Measurement setup using the 10 dB attenuator as object of interest

Figure 5.3 the difference between the transmission coefficient obtained from the SDR measurement and the one measured with a VNA.

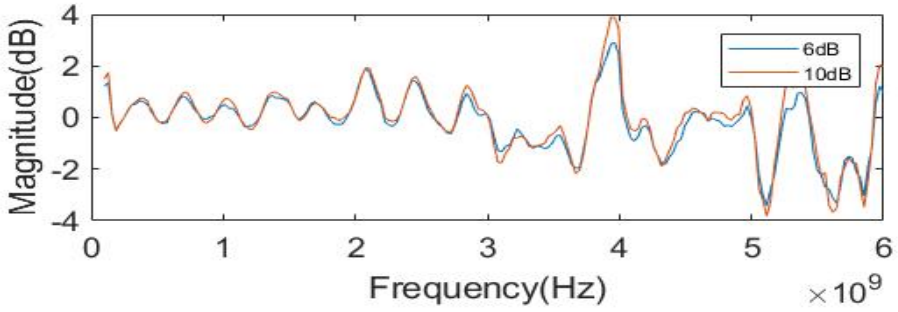

(a) Magnitude of difference between the transmission coefficients

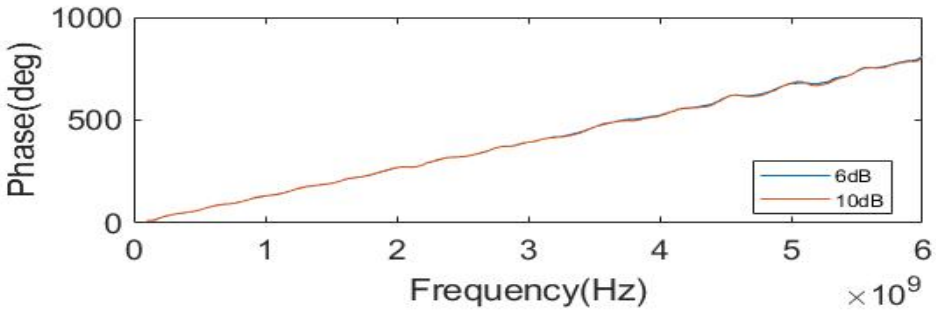

(b) Phase of difference between the transmission coefficients

Figure 5.3: Magnitude and phase of difference between the transmission coefficients using 6 dB and 10 dB attenuators as objects

It can be seen that the difference, between the magnitude obtained with the SDR measurement, and the magnitude obtained with the VNA is less than 1 dB difference for frequencies under 3 GHz. On the contrary, the phase estimated with the SDR is different from the phase estimated with the VNA.

To further investigate this phase error source, some calibration strategies can be implemented. The first setup that will be used is displayed in Figure 5.4. The transmission coefficients obtained with only cables will be used as calibration coefficients. Additionally, measurements using 6 dB attenuator as object and 10dB as object will also be used as calibration coefficients.

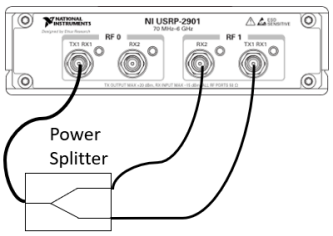

Figure 5.4: Measurement setup using no object (cables)

The calibration coefficients will be subtracted from the measurements obtained

while using the 6 dB attenuator as object, the results of this operation are showed in Figure 5.5. It can be seen that the results using the calibration coefficients obtained with the cables, have a really oscillatory behaviour. The results using the calibration coefficients obtained with the attenuators are very similar to the measurements of the VNA.

Figure 5.6 displays the results of subtracting the calibration coefficients from measurements done with the 10 db attenuator as object. Similar results can be seen in these measurements. The calibration done with the 6 db and 10 db measurements give a better result that the calibration done with only cables.

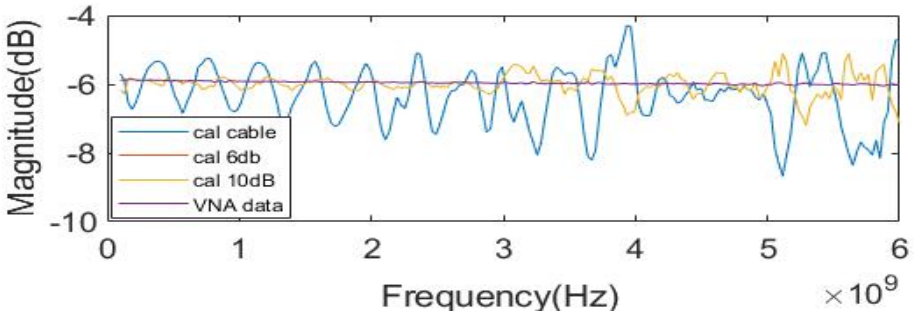

(a) Magnitude of measurement using 6 dB as object

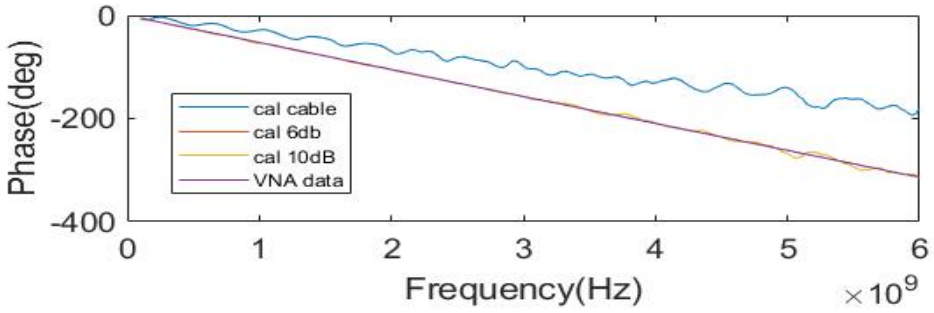

(b) Phase of measurement using 6 dB as object

Figure 5.5: Measurement using 6 dB as object with three different calibration coefficients

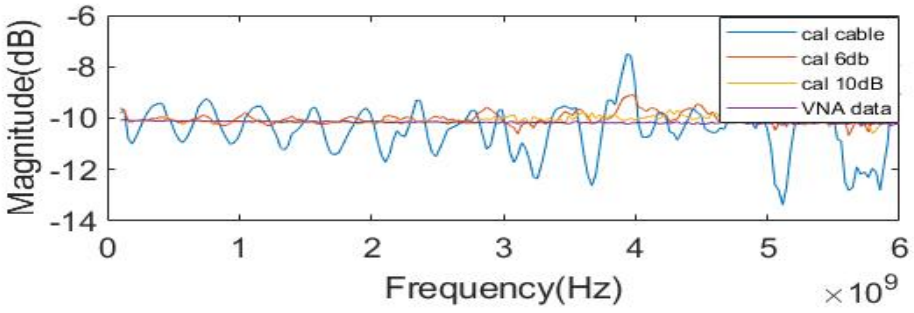

(a) Magnitude of measurement using 10 dB as object

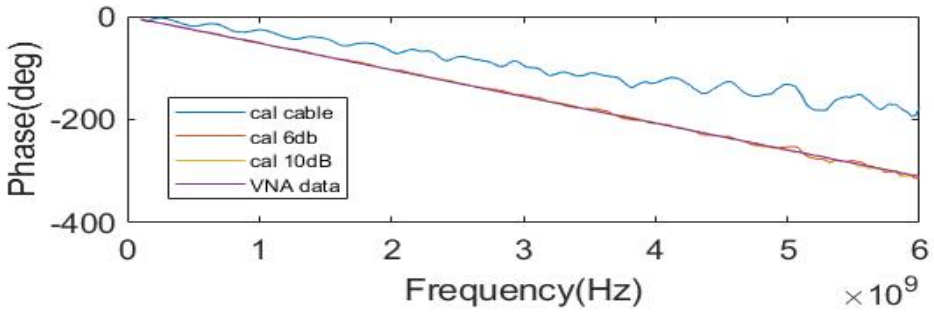

(b) Phase of measurement using 10 dB as object

Figure 5.6: Measurement using 10 dB as object with three different calibration coefficients

5.2 Antenna measurements

We investigated the measurement accuracy of a real microwave imaging antenna system, as shown in Figure 5.7. This imaging tank is composed of 20 monopole antennas that evenly distributed in a circle of radius 20 cm.

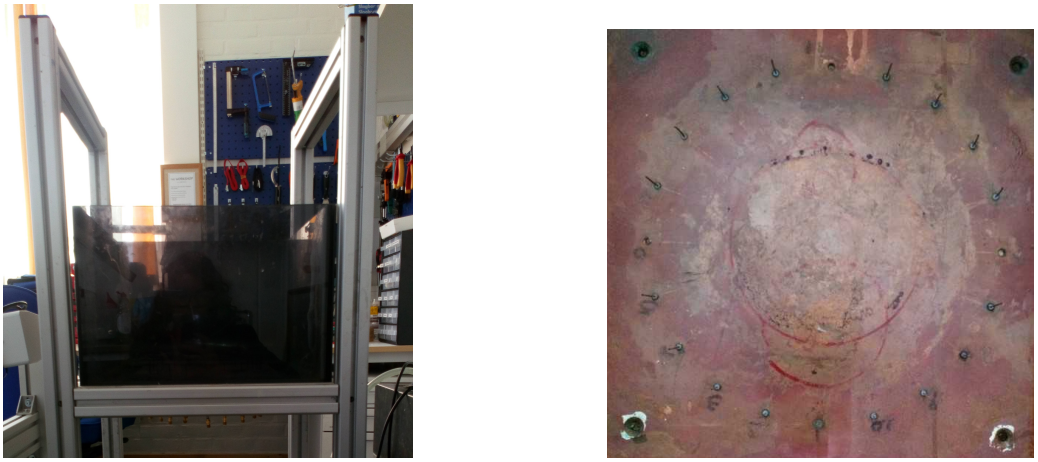

(a) Side view of imaging tank **(b)** Antenna array inside imaging tank

Figure 5.7: Picture of imaging tank used for measurements

The transmission coefficient between different antennas pairs were estimated from SDR measurement and compared with the VNA data. Figure 5.8 shows the magnitude results obtained with an adjacent antenna pair. Figure 5.10 show the magnitude results obtained with the most distant antenna pair. It can be seen that the magnitude response from the adjacent antenna pair is similar to the object magnitude response obtained with the VNA. Particularly in frequencies under 3GHz. However, the phase is different (as seen in Figure 5.9). This is the same behaviour seen in the measurements using attenuators as objects. In the most distant antenna pair the quality of the estimation decrease. There is also a phase difference between the estimation and the VNA data (Figure 5.11).

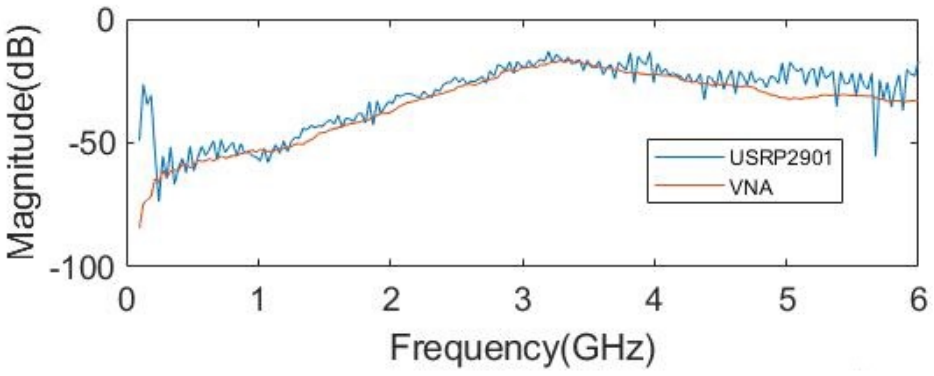

Figure 5.8: Adjacent antenna pair response obtained with SDR and VNA

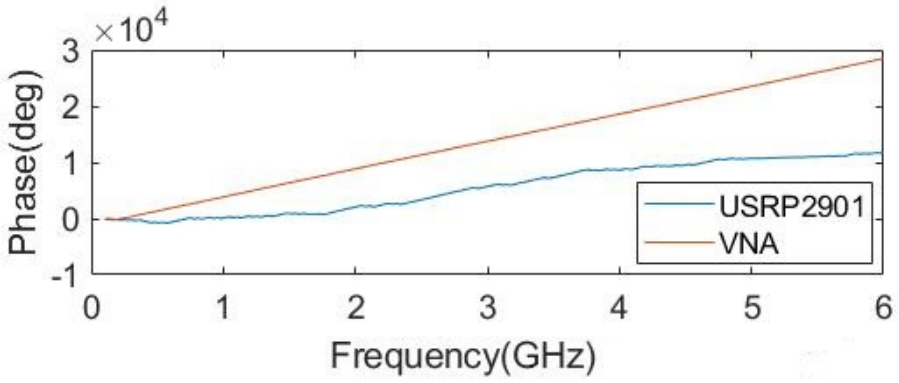

Figure 5.9: Phase of adjacent antenna pair response obtained with SDR and VNA

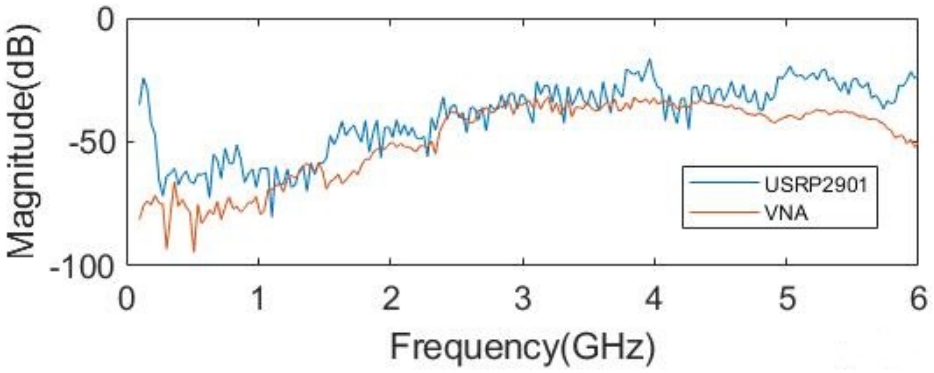

Figure 5.10: Most distant antenna pair response obtained with SDR and VNA

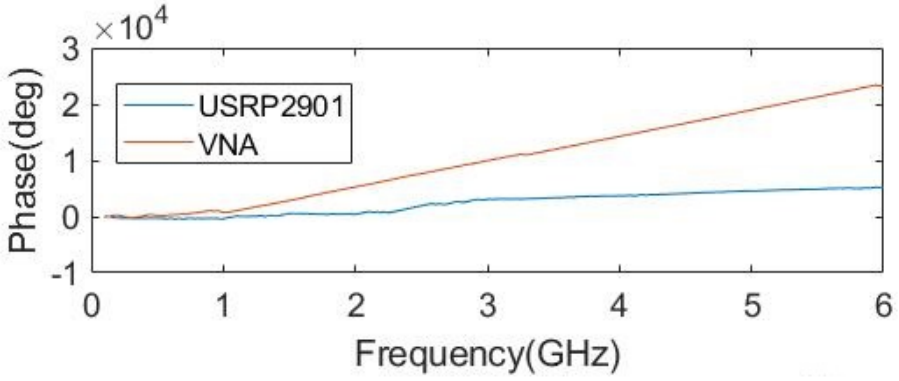

Figure 5.11: Phase of most distant antenna pair response obtained with SDR and VNA

5.3 Discussion

After studying the possible reasons for these results, it was found that the reflection coefficient is very high in the ports of the SDR board. Furthermore, the reflection coefficient changes when the port is in active state and when it is in inactive state as seen in Figure 5.12.

The decrease in magnitude in the received signals (Section 4.1) can also be explained by the increase of the reflection coefficient in higher frequencies. This means there will always be a decrease in quality of the results in higher frequencies.

This makes the calibration more difficult, because this means that a great part of the signal will be reflected back and leaked between the ports. The current power splitter, presents a 20dB isolation, which is not enough to attenuate the effect of the signals. This explains the difference between the phase estimated with SDR measurements and the phase obtained from VNA data, as seen in Figure 5.3.

It can be seen in Figure 5.5 that the calibration of the phase difference is more accurate if the object used for the calibration coefficients is similar to the object being measured. The same can be said for the results shown in Figure 5.6. The calibration coefficients obtained using the setup shown in Figure 5.4, display an oscillatory behaviour. This happens because the leaked signal is stronger.

In Figure 5.8 and Figure 5.10, it can be seen that the magnitude of the received signals decrease the farther away the antennas are. This makes the results more vulnerable to noise in the most distant pair.

One way to resolve this issue would be to take into account the effect that the leakage is creating into the calculations from the calibration, and another one would be to have more isolation in the connecting devices.

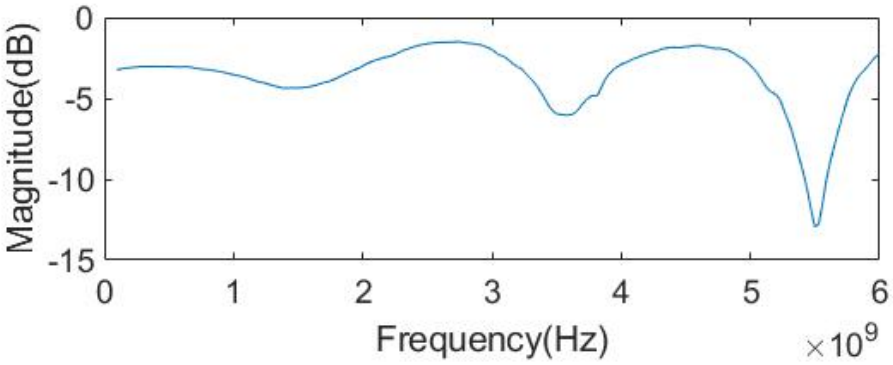

(a) Reflection coefficient of port Tx/Rx1 at inactive state

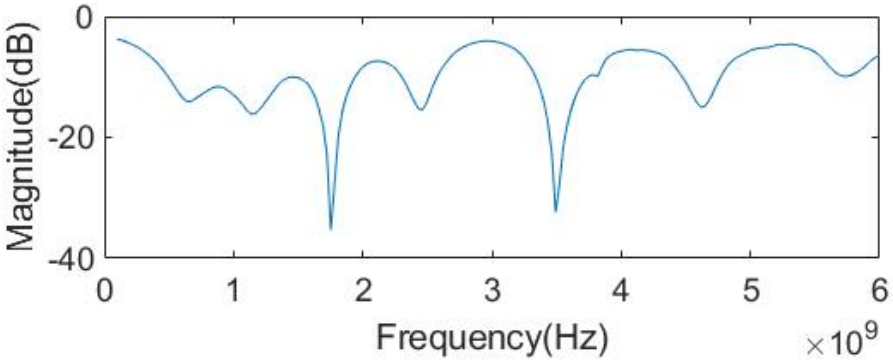

(b) Reflection coefficient port Tx/Rx1 at active state

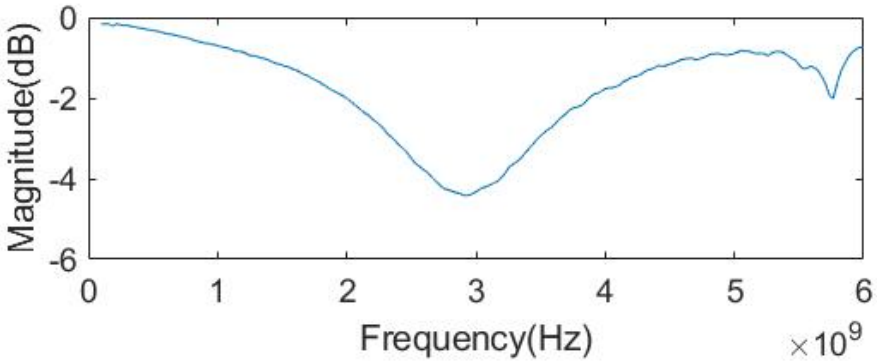

(c) Reflection coefficient port Rx2 at inactive state

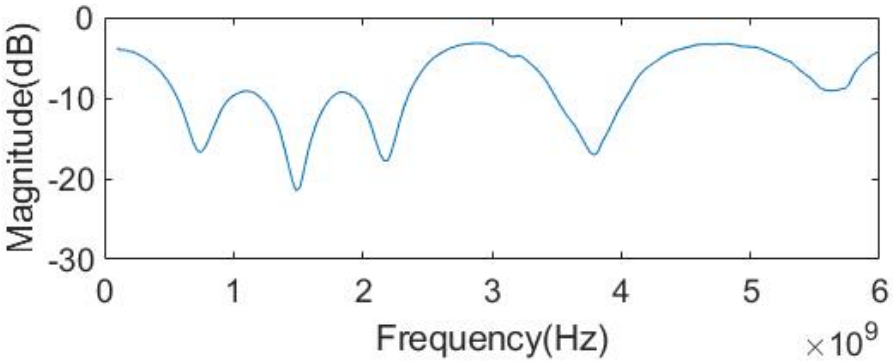

(d) Reflection coefficient port Rx2 at active state

Figure 5.12: Measured reflection coefficient at the RF ports of the SDR board

6
Other Applications

Given the flexibility of the SDR, it can also be used for other medical applications, like non contact measurement of respiration and heartbeat rate. Respiration rate and heartbeat rate are important physiological variables for the human being. The monitoring of this parameters becomes crucial in medical applications and rescue missions, where doppler radars can be used for the through-obstacle detection of respiration and heartbeat rate, achieving easier and fast localization of survivors in earthquake rubble. Usually a doppler radar senses motion by transmitting a radio wave signal, and receiving the motion-modulated signal that was reflected from the target. The reflected wave is frequency modulated by the periodic movements on the surface of the chest generated by respiration and heart movements. If the radar is illuminating the whole chest at once, the detected motion will be an average of all displacement in the area [39]. The amplitude of the chest displacement is expected to be around 10mm for respiration and 0.1mm for heart activity [40].

6.1 Method

The experiment was conducted with only one person sitting or standing (Figure 6.1), with the radar located in the same height as the chest. The distance between the radar and the person could be adjusted during experiments [39, 41].

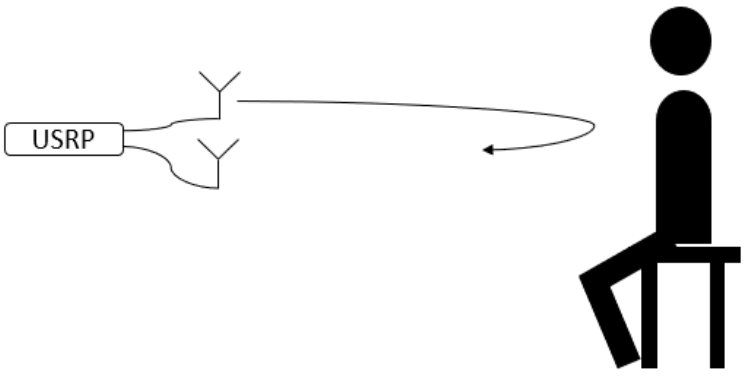

Figure 6.1: Basic test scenario for vital sign detection.

A metronome was used to have a reference measurement of the respiration rate. The reference respiration rate is 16 BPM. No reference data was obtained for the heartbeat rate.

The measurements will have a duration of 30s to make sure to get a whole period of the respiration and heartbeat signals. Since the healthy adult breathes from 12-20 times per minute, the signal will be filtered with a butterworth band pass filter of 6th order with the range between 0.15 Hz and 0.5 Hz (9-30 breaths per minute), to obtain the respiration signal. The resting heartbeat of a healthy adult is in the range 60-100 beats per minute, so the received signal will also be filtered with a filter with range between 0.9Hz and 2.5 Hz (54-150 beats per minute).

Two methods will be used to find the respiration and heartbeat rate of the filtered and normalized signals, the FFT, and the Auto-correlation. The FFT of the signal will be taken and the maximum value (peak) in the frequency domain will represent the frequency of respiration or heartbeat rate. The Auto-correlation can also be used to detect the presence of the period and determine their duration, since the auto-correlation sequence of a periodic signal has the same periodic characteristics as the signal [42]. In the auto-correlation the first peak (p1), after the main peak in located in 0, will indicate the periodicity of the signal. The respiration's rate can be found with the following formula (a detailed explanation of this principle is discussed in [42]):

$$f_{p_1} = \frac{60}{t_{(p_1)}}, \tag{6.1}$$

where f_{p1} is the respiration rate and $t_{(p_1)}$ is the time in seconds it takes for p_1 to occur in the auto-correlation signal.

6.2 Results

Figure 6.2 displays the reflected signal received by the board after being modulated by the chest displacement of the subject.

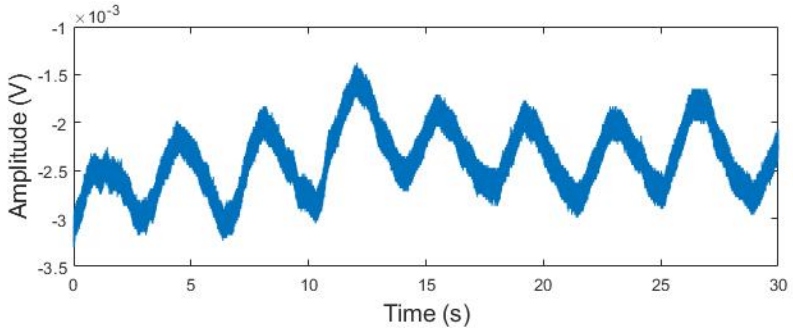

Figure 6.2: Received signal.

It is noticeable that the signal has a periodical pattern. It must be noted that the information from the displacement generated from respiration and displacement generated by the heartbeat are both included in this signal, in other words, it is the sum-up of the total displacement on the chest area. This signal is filtered with the respiration filter, and the resulting signal is shown in Figure 6.3a. Looking at the signal, 8 periods in 30 s can be counted, meaning that the respiration rate is of 16 breaths per minute.

Figure 6.3b shows the signal in time domain and the FFT of the signal. It can be seen that the peak is located in 16 breaths per minute, confirming that the estimation of the respiration rate with the SDR measurements is correct.

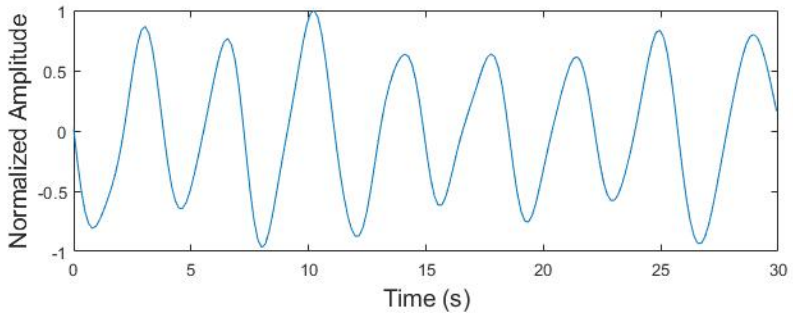

(a) Time domain signal.

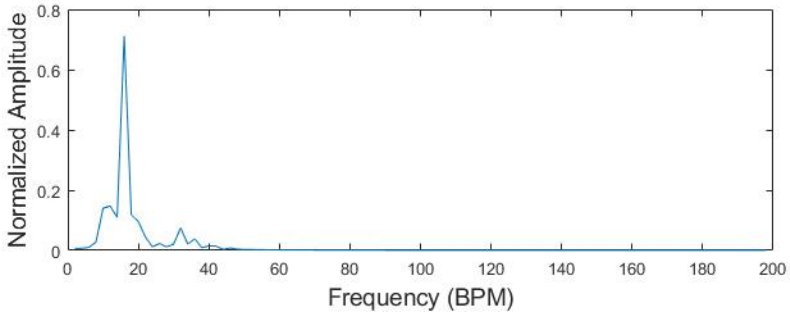

(b) Frequency domain signal.

Figure 6.3: Signal After respiration filer in Time domain and Frequency domain.

The auto-correlation is also used to determine the respiration rate, the result from auto-correlating the filtered and normalized signal is shown in Figure 6.4.

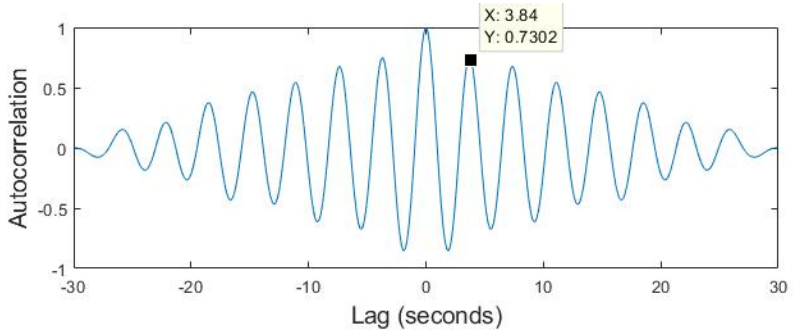

Figure 6.4: Auto-correlation of respiration.

The first peak is in 3.84s, using Equation 6.1 the respiration rate can be found. The resulting respiration rate is 16.3 breaths per minute which is a number close to the appropriate respiration rate. The signal filtered with the heart beat filter is displayed in Figure 6.5 in time domain and frequency domain. In the frequency Domain it can be seen that a peak is found in 82 beats per minute indicating this is a possible value of the heartbeat rate. This is an expected value since the normal rate for adults is from 60 to 100 beats per minute.

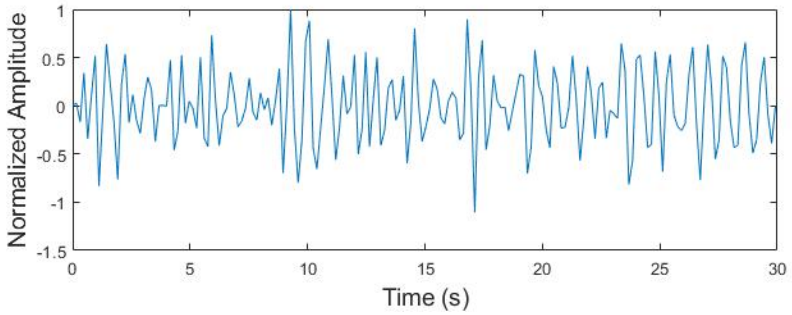

(a) Time domain signal.

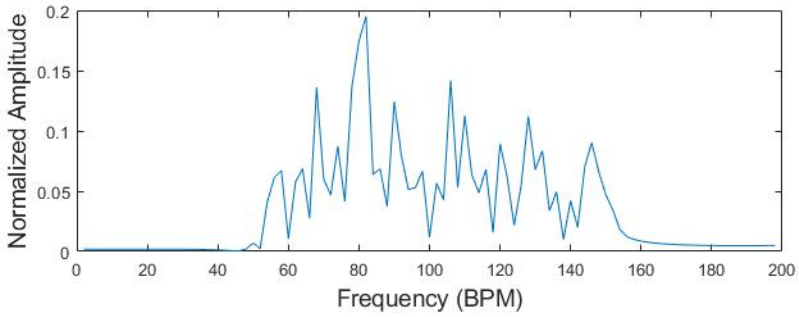

(b) Frequency Domain signal.

Figure 6.5: Signal After Heartbeat filer in Time domain and Frequency domain

6.3 Discussion

The respiration rate and heartbeat rate were correctly estimated using the SDR measurements. The testing environment will have an effect of the data received, if there is more than one person in the way of the radar, the signals get mixed and it is difficult to separate them.

The advantage of the auto-correlation method is that even if the signal is shorter in time, it will be able to find the respiration rate, since it only needs one period of the signal to find the periodicity. It is also more robust against noise than the FFT method. This is useful if rapid measurements are needed, such as real time monitoring of the vital signs of elderly people.

7
Conclusion

This study set out to investigate the feasibility of using SDR for microwave-based medical applications. As part of this research, three different calibration strategies were implemented and tested to attempt to fix the random phase problem encountered due to the use of different PLLs in the transmitter and the receiver in the SDR technology. Among the calibration strategies tested, it was found that strategy 1 performed better than strategy 2 and strategy 3. With this strategy, a good measurement repeatability was obtained, which could allow the device to be used for medical monitoring.

The measurement accuracy, however, is affected by the strong reflection of the RF ports of the SDR board. A more effective calibration approach needs to be developed in order to improve the measurement accuracy. Furthermore, it was shown that the SDR technology has a great potential to be used for non-contact vital sign monitoring at a distance.

7.1 Future Work

Due to the limitations set by the reflection coefficients in the ports of the SDR it would be interesting to further develop the calibration methods to improve the measurement accuracy. One approach is to take the effect of leakage into account in the calibration and the other approach is to increase the isolation in the devices used for the calibration. This would decrease the leaked signal from port to port, allowing for the simple calibration method to estimate the absolute phase. Imaging test was missing in this report and it is interesting to perform the test after the accuracy of the measurements is improved.

Bibliography

[1] Andreas Fhager, Stefan Candefjord, Mikael Elam, and Mikael Persson. Microwave diagnostics ahead: Saving time and the lives of trauma and stroke patients. *IEEE Microwave Magazine*, 19(3):78–90, 2018.

[2] Conceicao Raquel Cruz, Johan Jacob Mohr, and Martin OHalloran. *An Introduction to Microwave Imaging for Breast Cancer Detection*. Springer International Publishing, 2018.

[3] A. Fhager, P. Hashemzadeh, and M. Persson. Reconstruction quality and spectral content of an electromagnetic time-domain inversion algorithm. *IEEE Transactions on Biomedical Engineering*, 53(8):1594–1604, 2006.

[4] Maryam Naseri. Microwave tomography for breast cancer detection. Master's thesis, Chalmers University f technology, 2015.

[5] T. S. England. Dielectric properties of the human body for wave-lengths in the 1–10 cm. range. *Nature*, 166(4220):480–481, 1950.

[6] A.j. Surowiec, S.s. Stuchly, J.r. Barr, and A. Swarup. Dielectric properties of breast carcinoma and the surrounding tissues. *IEEE Transactions on Biomedical Engineering*, 35(4):257–263, 1988.

[7] K R Foster, J L Schepps, R D Stoy, and H P Schwan. Dielectric properties of brain tissue between 0.01 and 10 ghz. *Physics in Medicine and Biology*, 24(6):1177–1187, 1979.

[8] A Peyman, S J Holden, S Watts, R Perrott, and C Gabriel. Dielectric properties of porcine cerebrospinal tissues at microwave frequencies:in vivo,in vitroand systematic variation with age. *Physics in Medicine and Biology*, 52(8):2229–2245, 2007.

[9] Rachael I. Scahill, Chris Frost, Rhian Jenkins, Jennifer L. Whitwell, Martin N. Rossor, and Nick C. Fox. A longitudinal study of brain volume changes in normal aging using serial registered magnetic resonance imaging. *Archives of Neurology*, 60(7):989, 2003.

[10] Serguei Semenov, Toan Huynh, Thomas Williams, Brian Nicholson, and Anna Vasilenko. Dielectric properties of brain tissue at 1ghz in acute ischemic stroke: Experimental study on swine. *Bioelectromagnetics*, 38(2):158–163, 2016.

[11] Puyan Mojabi, Majid Ostadrahimi, Lotfollah Shafai, and Joe Lovetri. Microwave tomography techniques and algorithms: A review. *2012 15 International Symposium on Antenna Technology and Applied Electromagnetics*, 2012.

[12] Johan Köster. Image reconstruction and fdtd modelling of an antenna array for 3d microwave tomography. Master's thesis, Chalmers University of technology, 2011.

[13] Hooi Been Lim, Nguyen Thi Tuyet Nhung, Er-Ping Li, and Nguyen Duc Thang. Confocal microwave imaging for breast cancer detection: Delay-multiply-and-sum image reconstruction algorithm. *IEEE Transactions on Biomedical Engineering*, 55(6):1697–1704, 2008.

[14] Beadaa Jasem Mohammed. *Design and implementation of microwave imaging systems for medical applications*. PhD thesis, The University of Queensland, Australia, 2014.

[15] Joshua Chong Yue Lai, Cheong Boon Soh, Erry Gunawan, and Kay Soon Low. Uwb microwave imaging for breast cancer detection — experiments with heterogeneous breast phantoms. *Progress In Electromagnetics Research M*, 16:19–29, 2011.

[16] James.R.Andrews. *Picosecond Pulse Generator for Uwb Radars*. Picosecond Pulse Lab, application note an-9 edition, 2000.

[17] Xuezhi Zeng. *Time domain systems for microwave imaging: accuracy evaluations and prototype design*. PhD thesis, Chalmers, 2013.

[18] Cemin Zhang and Aly Fathy. Reconfigurable pico-pulse generator for uwb applications. *2006 IEEE MTT-S International Microwave Symposium Digest*, 2006.

[19] J. Marimuthu, K.s. Bialkowski, and A.m. Abbosh. Reconfigurable software defined radar for medical imaging. *2014 1st Australian Microwave Symposium (AMS)*, 2014.

[20] Anthony E. Stancombe and Konstanty S. Bialkowski. Portable biomedical microwave imaging using software- defined radio. *2018 Asia-Pacific Microwave Conference (APMC)*, 2018.

[21] Cam Nguyen and Jeongwoo Han. Time-domain ultra-wideband radar, sensor and components. *SpringerBriefs in Electrical and Computer Engineering*, 2014.

[22] James.R.Andrews. *Picosecond Pulse Generator techniques and pulser capabilities*. Picosecond Pulse Lab, application note an-19 edition, 2008.

[23] Lianfeng Zou, Shulabh Gupta, and Christophe Caloz. A simple picosecond pulse generator based on a pair of step recovery diodes. *IEEE Microwave and Wireless Components Letters*, 27(5):467–469, 2017.

[24] Jianming Zhou, Qiuyuan Lu, Fan Liu, and Yinqiao Li. A novel picosecond pulse generation circuit based on srd and nltl. *Plos One*, 11(2), 2016.

[25] J.s. Lee and C. Nguyen. Uniplanar picosecond pulse generator using step-recovery diode. *Electronics Letters*, 37(8):504, 2001.

[26] D. Williams, P. Hale, and K.a. Remley. The sampling oscilloscope as a microwave instrument. *IEEE Microwave Magazine*, 8(4):59–68, 2007.

[27] Maxim Integrated. *Multiply Your Sampling Rate with Time-Interleaved Data Converters*, tutorial 989 edition, 2001.

[28] Keysight Technologies. *What is the difference between an equivalent time sampling oscilloscope and a real-time oscilloscope?*, application note1608 edition.

[29] Ian Hickman. *Oscilloscopes: how to use them, how they work*. Elsevier, 2001.

[30] Changzhi Li Changzhan Gu. From tumor targeting to speech monitoring: Accurate respiratory monitoring using medical continuous-wave radar sensors. *IEEE Microwave Magazine*, 15(4):66–76, 2014.

[31] Adrian Figueroa, Belal Al-Qudsi, Niko Joram, and Frank Ellinger. Comparison of two-way ranging with fmcw and uwb radar systems. *2016 13th Workshop on Positioning, Navigation and Communications (WPNC)*, 2016.

[32] Cam Nguyen and Joongsuk Park. Stepped-frequency radar sensor analysis. *Stepped-Frequency Radar Sensors SpringerBriefs in Electrical and Computer Engineering*, page 39–64, 2016.

[33] Stephanie Hamill. Introduction to sdr - wireless innovation forum.

[34] What is ni usrp hardware?

[35] Donald R. Wehner, Bruce Barnes, Benjamin C. Flores, and Donald R. Wehner. *High-resolution radar*. Artech House, 1996.

[36] David Andrew Noon. *Stepped-Frequency Radar Design and Signal Processing Enhances Ground Penetrating Radar Performance*. PhD thesis, The University of Queensland, Queenslan, 1996.

[37] National Instruments. *AN INTRODUCTION TO SOFTWARE DEFINED RADIO With NI LabVIEW and NI USRP*. 2013.

[38] Analog Devices. Rf agile transceiver ad9361, 2013.

[39] Olga Boric-Lubecke, Wansuree Massagram, Victor M. Lubecke, Anders Host-Madsen, and Branka Jokanovic. Heart rate variability assessment using doppler radar with linear demodulation. *2008 38th European Microwave Conference*, 2008.

[40] T. Kondo, T. Uhlig, P. Pemberton, and P. D. Sly. Laser monitoring of chest wall displacement. *European Respiratory Journal*, 10(8):1865–1869, 1997.

[41] Hongming Shen, Chen Xu, Yongjie Yang, Ling Sun, Zhitian Cai, Lin Bai, Edward Clancy, and Xinming Huang. Respiration and heartbeat rates measurement based on autocorrelation using ir-uwb radar. *IEEE Transactions on Circuits and Systems II: Express Briefs*, 65(10):1470–1474, 2018.

[42] Guanghao Sun and Takemi Matsui. Rapid and stable measurement of respiratory rate from doppler radar signals using time domain autocorrelation model. *2015 37th Annual International Conference of the IEEE Engineering in Medicine and Biology Society (EMBC)*, 2015.

[43] Configuration:advanced:lo frequency property.

A

Appendix 1

A.1 LO functionality block

The USRP includes DC offset correction in the RFIC AD9361, which will use a filter to eliminate any DC components. This is a desirable trait in communications systems to prevent bit errors from happening, but in order to send a sinusoid of 0Hz, the LO frequency needs to be configured.

The carrier frequency is obtained in hardware by combining the frequency translation on the local oscillator (LO) and the additional frequency translation in the digital signal processing on the FPGA [43].

If only the value of the carrier frequency is specified, the NI-USRP will set the LO frequency as close as possible to the carrier frequency and then carry out the rest of the frequency translation using the Digital Signal Processor(DSP) in the FPGA.

The difference between the LO frequency and the carrier frequency cannot be greater than half the device bandwidth, since the DSP of the FPGA will not be able to process the rest of the signal due to a lack of sufficient bandwidth.

Taking everything into account, the LO frequency needs to be configured to a value far enough from the carrier frequency that the DC offset correction in the AD9361 will not filter it out, but still close enough that the bandwidth of the Digital signal processor will be able to process the remaining signal.

To prove how the filtering of the DC signal works, a simple experiment can be conducted using the configuration shown in Figure 4.1.

A signal of frequency 0Hz and amplitude 0,7 will be sent (shown in Figure A.1), the carrier frequency (f_c) will then be configured to be 915MHz and the LO frequency (f_{lo}) will not be configured, thus, allowing the NI-USRP to choose an LO frequency as close to 915M as possible.

Figure A.2a shows the received signal, both I and Q signals are filtered out by the DC correction filter in the AD9361 since the signal just goes to amplitude 0. Likewise, Figure A.2b shows the power spectrum of the signal, since nothing was received, it can be seen that the power is at a value of -80dB.

By experimenting with different values, it was found that the value $f_c - f_{lo}$ =5MHz was a good difference between the carrier frequency and LO frequency. This conclusion was reached, since the 5MHz signal is different enough from being a DC signal,that it will not be filtered out, but small enough that the Digital signal processor from the FPGA will be able to process it.

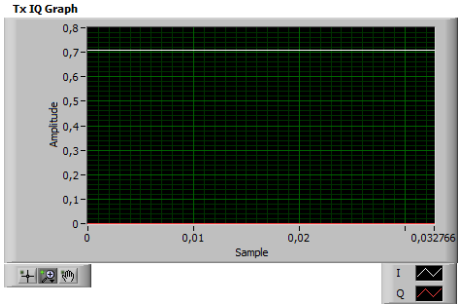

Figure A.1: Sinusoid signal with 0Hz and amplitude 0,7

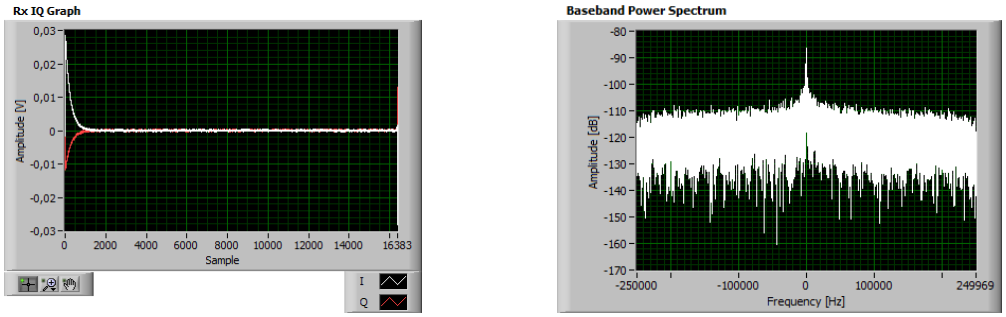

(a) Received signal **(b)** Power Spectrum

Figure A.2: Received signal while not configuring the LO frequency

the previous experiment is repeated, but this time using $f_c - f_{lo}$ =5MHz, meaning that the LO frequency is configured to be f_{lo} =910MHz, since the carrier frequency is f_c=915MHz.The results are displayed in Figure A.3 .

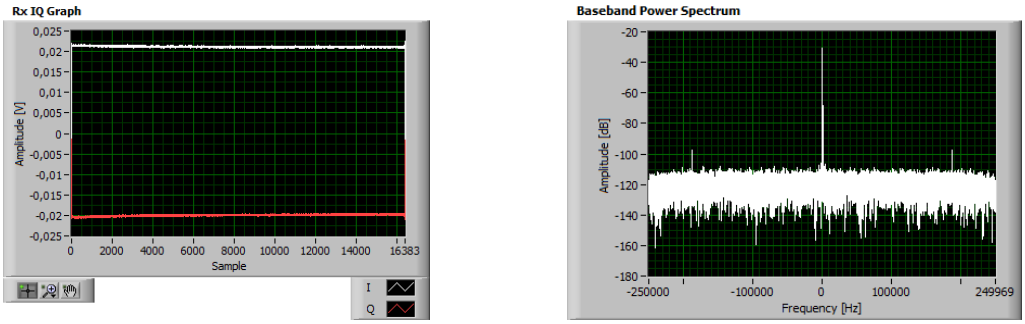

(a) Received signal **(b)** Power Spectrum

Figure A.3: Received signal while not configuring the LO frequency

The Received signal can be seen in Figure A.3a,the DC signal is now received and down-converted without problems.The power spectrum of the received signal when configuring the LO frequency is shown in Figure A.3b.The power is at a value of -20dB.